Int J Appl Earth Obs Geoinformation 91 (2020) 102136

Contents lists available at ScienceDirect

Int J Appl Earth Obs Geoinformation

journal homepage: www.elsevier.com/locate/jag

Investigation and validation of algorithms for estimating land surface temperature from Sentinel-3 SLSTR data

Jiajia Yang[a], Ji Zhou[a,*], Frank-Michael Göttsche[b], Zhiyong Long[c], Jin Ma[a], Ren Luo[a]

[a] School of Resources and Environment, Center for Information Geoscience, University of Electronic Science and Technology of China, Chengdu 611731, China
[b] Institute of Meteorology and Climate Research, Karlsruhe Institute of Technology, Karlsruhe, 76344, Germany
[c] College of Meteorology and Oceanography, National University of Defense Technology, Nanjing, 211101, China

ARTICLE INFO

Keywords:
Land surface temperature (LST)
Split-window algorithm (SWA)
Sentinel-3 SLSTR
Validation

ABSTRACT

Land surface temperature (LST) is an important indicator of global ecological environment and climate change. The Sea and Land Surface Temperature Radiometer (SLSTR) onboard the recently launched Sentinel-3 satellites provides high-quality observations for estimating global LST. The algorithm of the official SLSTR LST product is a split-window algorithm (SWA) that implicitly assumes and utilizes knowledge of land surface emissivity (LSE). The main objective of this study is to investigate alternative SLSTR LST retrieval algorithms with an explicit use of LSE. Seventeen widely accepted SWAs, which explicitly utilize LSE, were selected as candidate algorithms. First, the SWAs were trained using a comprehensive global simulation dataset. Then, using simulation data as well as *in-situ* LST, the SWAs were evaluated according to their sensitivity and accuracy: eleven algorithms showed good training accuracy and nine of them exhibited low sensitivity to uncertainties in LSE and column water vapor content. Evaluation based on two global simulation datasets and a regional simulation dataset showed that these nine SWAs had similar accuracy with negligible systematic errors and RMSEs lower than 1.0 K. Validation based on *in-situ* LST obtained for six sites further confirmed the similar accuracies of the SWAs, with the lowest RMSE ranges of 1.57–1.62 K and 0.49 − 0.61 K for Gobabeb and Lake Constance, respectively. While the best two SWAs usually yielded good accuracy, the official SLSTR LST generally had lower accuracy. The SWAs identified and described in this study may serve as alternative algorithms for retrieving LST products from SLSTR data.

1. Introduction

Land surface temperature (LST) is an important indicator associated with climatic, meteorological, hydrological and environmental phenomena and processes (Wan and Dozier, 1996; Weng, 2009). It is widely used in climate change investigation (Tomlinson et al., 2011), hydrological process modelling (Kalma et al., 2008), drought monitoring (Wan et al., 2004), and fire risk assessment (Guo and Zhou, 2004). LST is affected by or depends on many factors, such as land surface type, surface moisture, illumination and atmospheric conditions; thus, it is difficult to obtain *in-situ* LST that are presentative of large areas (Ermida et al., 2014; Guillevic et al., 2017.), e.g. satellite pixel. In contrast, satellite thermal infrared (TIR) remote sensing has the advantage of wide coverage and the ability to perform regular revisits of a site. Therefore, satellite TIR remote sensing is widely employed for estimating LST (Chatterjee et al., 2017; Ren et al., 2018; Wang et al., 2019; Zheng et al., 2019; Zhang et al., 2019). In the past four decades, the scientific community has successfully developed numerous LST retrieval algorithms (Li et al., 2013a), e.g. the well-known single channel algorithm (Jiménez-Muñoz, 2003), day/night algorithm (Wan and Li, 1997), mono-window algorithm (Qin et al., 2001) and generalized split-window (GSW) algorithm (Wan and Dozier, 1996).

Sentinel-3 is an important component of the European Space Agency's Copernicus Earth monitoring system and consists of three satellites (3A, 3B, and 3C). Sentinel-3A and Sentinel-3B were successfully launched in February 2016 and April 2018, respectively, while the launch of Sentinel-3C is still under planning. Sentinel-3 satellites have sun-synchronous orbits with an orbit height of 814.5 km. The repeat period of each Sentinel-3 satellite is 27 days. Sentinel-3 carries the Sea and Land Surface Temperature Radiometer (SLSTR), which like its predecessor AATSR onboard ENVISAT has oblique and near nadir view modes. Furthermore, SLSTR has a wider swath (750 km in dual view

* Corresponding author at: No.2006, Xiyuan Ave, West Hi-Tech Zone, Chengdu 611731, Sichuan, China.
E-mail addresses: yangjiajia0606@163.com (J. Yang), jzhou233@uestc.edu.cn (J. Zhou), frank.goettsche@kit.edu (F.-M. Göttsche), longzy@aliyun.com (Z. Long), majin@std.uestc.edu.cn (J. Ma), luoren@std.uestc.edu.cn (R. Luo).

https://doi.org/10.1016/j.jag.2020.102136
Received 30 December 2019; Received in revised form 16 April 2020; Accepted 19 April 2020
Available online 29 April 2020

and 1400 km in single view) and, therefore, achieves a higher observation frequency. With its single view swath width SLSTR provides a mean global coverage revisit time at the equator of 1 day (one spacecraft) or half a day (two spacecraft). SLSTR is a high accuracy infrared radiometer and provides reliable global sea surface temperature and LST observations (Coppo et al., 2010). It has six visible/near infrared/shortwave infrared channels (i.e. S1 – S6; spatial resolution: 500 m) and three TIR channels (i.e. S7 – S9; spatial resolution: 1 km). The central wavelengths of S8 and S9 are 10.85 μm and 12 μm, respectively. These two SLSTR channels have similar spectral responses as the 11 μm and 12 μm channels of NOAA AVHRR, Terra/Aqua MODIS and ENVISAT AATSR, thereby allowing the LST estimation through the split-window algorithms (SWA). The basic principle underlying SWAs is to utilize the different atmospheric absorptions in two adjacent TIR channels (i.e. near 11 μm and 12 μm) to eliminate atmospheric effects; however, SWAs require a priori knowledge of land surface emissivity (LSE) in these two channels (Coll et al., 1994; Wan and Dozier, 1996; Jiang and Liu, 2014; Jiang and Li, 2008; Tang et al., 2008; Ye et al., 2017).

The official SLSTR LST retrieval algorithm is a SWA that uses LSE implicitly and has been adapted from the ENVISAT AATSR LST algorithm (Ghent et al., 2017; Prata, 2002). This algorithm differs from most other operational satellite LST retrieval algorithms, e.g. for MODIS (i.e. M*D11), VIIRS and Chinese Fengyun-3 VIRR products (Wan and Dozier, 1996; Yu et al., 2005; Jiang et al., 2013; Tang et al., 2015), which use LSEs explicitly and have been assessed favorably by several authors (Freitas et al., 2010; Guillevic et al., 2014; Wan, 2014). In comparison, SWAs using LSE implicitly are prone to be more strongly affected by uncertainties in land cover classification, which generally forms the basis for determining a pixel's LSE (Coll et al., 2012; Peres and DaCamara, 2005; Prata, 2002).

The primary objective of this study is to adjust several well-established SWAs that use LSE explicitly for estimating LST from SLSTR data. The SWAs are then comprehensively evaluated with simulation datasets and *in-situ* LST datasets and compared to the official SLSTR LST algorithm. Therefore, this study also helps to assess the maturity of the official SLSTR LST product.

2. Datasets

2.1. Sentinel-3 data

SLSTR data products have three processing levels (i.e. Level-0, Level-1 and Level-2) of which Level-1 and Level-2 are publically available. Level-1 products consist of calibrated radiances and brightness temperatures (RBT) for each channel at the instrument grid for nadir and oblique view, as well as some ancillary data. Among others, Level-2 products include sea surface temperature (SST), LST and fire radiative power (Sentinel-3 team, 2013). Angular effects on directional temperature and emissivity are difficult to estimate and dual-angle algorithms are less accurate even over topographically flat and homogeneous surfaces (Coll et al., 2006; Remedios et al., 2012). Hence, we use the nadir view SLSTR Level-1B products acquired between January 2017 and December 2018 to estimate LSTs from SLSTR. The Level-1B product is an output from Level-1 processing and contains the full-resolution geolocation radiometric measurements for each view and channel. The Level-1 RBT product includes Top of Atmosphere (TOA) brightness temperature (BT) for S7 - S9 (3.74 μm–12 μm) and TOA radiances for S1 - S6 (0.56 μm–2.25 μm), as well as associated Sun zenith and azimuth angles, satellite zenith and azimuth angles and land surface elevation, etc. These datasets are provided in NetCDF format and were downloaded from the Copernicus Open Access Hub (https://www.copernicus.eu/).

SLSTR LST is an official Level-2 product and has a spatial resolution of 1 km. It provides LST estimates and some associated parameters, e.g. LST uncertainty, normalized difference vegetation index (NDVI), vegetation type (biome), atmospheric column water vapor content (CWVC) and parameters related to LST retrieval. The official SLSTR LST product is estimated with the following SWA, which makes implicit use of LSE (Remedios et al., 2012):

$$T_s = a_{f,i,pw} + b_{f,i}(T_{11} - T_{12})^{\frac{1}{\cos(\theta/m)}} + (b_{f,i} + c_{f,i})T_{12} \quad (1)$$

where T_s is LST in K; a, b, and c are coefficients; T_{11} and T_{12} are the BTs in S8 and S9, respectively; subscript f corresponds to vegetation fraction; i denotes vegetation type; pw is the CWVC; θ is the satellite zenith view angle; and m is a variable depending on θ.

2.2. Global atmospheric profiles

Developing globally applicable LST algorithms requires atmospheric profile data that are representative of global atmospheric variability. Atmospheric profiles provide information on the vertical distribution of some critical parameters, e.g. air temperature, water vapor and air pressure. An "ideal" dataset containing atmospheric and land surface conditions and associated at-sensor observations can be obtained by performing forward radiative transfer calculations for a range of LST values and convolving the calculated (TOA) radiances with the sensor's spectral response function. This "ideal" dataset can then be used to train empirical and semi-empirical LST retrieval algorithms. Here, we used the atmospheric profiles from the Global Atmospheric Profile Dataset (GAPD) (Zhou et al., 2019), which was constructed from the SeeBor V5.0 dataset with 15,704 global profiles by quantifying the similarity between profiles and removing redundant profiles (Borbas et al., 2005). GAPD contains 549 global cloud-free profiles, with a CWVC range of $0.014 - 7.939\ g\ cm^{-2}$ and a near surface air temperature (NSAT) range of 224.25–309.05 K. GAPD has shown good representativeness of global atmospheric conditions in the training of the Global Land Surface Satellite (GLASS) LST retrieval algorithm (Zhou et al., 2019).

There are 4761 cloud-free atmospheric profiles over land in the SeeBor V5.0 dataset, which have CWVC values between 0.005 and $4.999\ g\ cm^{-2}$ and are not part of GAPD. These 4761 profiles were used to generate an independent dataset for evaluating the trained SWAs. In the subsequent evaluation, two further sources of atmospheric profiles were employed: the TIGR dataset (version Tigr2000_v1.2), which contains 2311 global profiles. Additional cloud checking reduced this number to 506, with CWVC ranging from 0.058 to $8.199\ g\ cm^{-2}$. The second source of atmospheric profiles was the Atmospheric Infrared Sounder (AIRS) AIRX2SUP product, which is obtained from combined observations of AIRS and the Advanced Microwave Sounding Unit (AMSU). This product has a spatial resolution of 45 km and provides atmospheric parameters (i.e. water vapor, air temperature and ozone) at 100 pressure levels between 1100.0 hPa and 0.0161 hPa (Olsen et al., 2007). Version 5 AIRX2SUP products between October 2011 and September 2012 over the Chinese landmass were downloaded from Goddard Earth Science Data and Information Center (GES DISC: http://daac.gsfc.nasa.gov). After additional cloud screening and quality checks, 14,532 AIRS profiles flagged as 'good' or 'highest' quality were available for further examination. These profiles were then screened based on their similarity, resulting in the final selection of 16 independent profiles over the Tibetan Plateau. The 16 selected profiles had CWVC values ranging from 0.015 to $0.041\ g\ cm^{-2}$ and were used to generate a regional simulation dataset. Considering the high elevation of the Tibetan Plateau and the low CWVC of these 16 AIRS profiles, these profiles can benefit a better understanding of the LST algorithms' performance in extremely dry conditions (Zhou et al., 2012). In the following, the above three evaluation datasets are referred to as ATP-S (SeeBor subset), ATP-T (TIGR subset) and ATP-A (AIRS subset) and are summarized together with the GAPD in Table 1.

2.3. In-situ LST

In order to examine the performance of LST retrieval algorithms in

Table 1
Atmospheric profile datasets used for evaluating the SWAs.

Name	Source	Number of profiles	CWVC range (g cm^{-2})	Region	Name of dataset (sample size)	Remark
GAPD	SeeBor V5.0	549	0.014 – 7.939	Global	TRA-G (3,162,240)	Training data
ATP-S	SeeBor V5.0	4761	0.005 – 4.999	Global	VAL-S (47,610)	Evaluation data; independent from GAPD
ATP-T	TIGR Tigr2000_v1.2	506	0.058 – 8.199	Global	VAL-T (5060)	Evaluation data
ATP-A	AIRX2SUP product	16	0.015 – 0.041	Tibetan Plateau	VAL-A (160)	Evaluation data

Note: (1) Description of TAR-G can be found in Section 3.1; and (2) Details about the forward simulation procedure for VAL-S, VAL-T and VAL-A are provided in Zhou et al. (2019).

Table 2
Details of the six validation sites.

Name of site	Longitude, Latitude	Elevation (m)	Land cover type	Instrument			Measurement	
				Model	Height (m)	Diameter of FOV (m)	Period	Interval (min)
Arou	100.46 °E, 38.05 °N	3033	Subalpine meadow	Kipp & Zonen CNR4	5	37	2017	10
Daman	100.37 °E, 38.86 °N	1556	Cropland	Eppley PIR	12	90	2017	10
Huazhaizi	100.32 °E, 38.77 °N	1731	Desert steppe	Kipp & Zonen CNR1	6	45	2017	10
Huangmo	100.99 °E, 42.11 °N	1054	Desert	Kipp & Zonen CNR1	6	45	2017	10
Gobabeb	15.05 °E, 23.55 °S	450	Gravel plain	KT15.85 IIP	25	4	2018	1
Lake Constance	9.44 °E, 47.61 °N*	395	Water	KT15.85 IIP	8	1.3	2018	3 (orig.: 15 s)

Note: * latitude and longitude centered on the ferry's route.

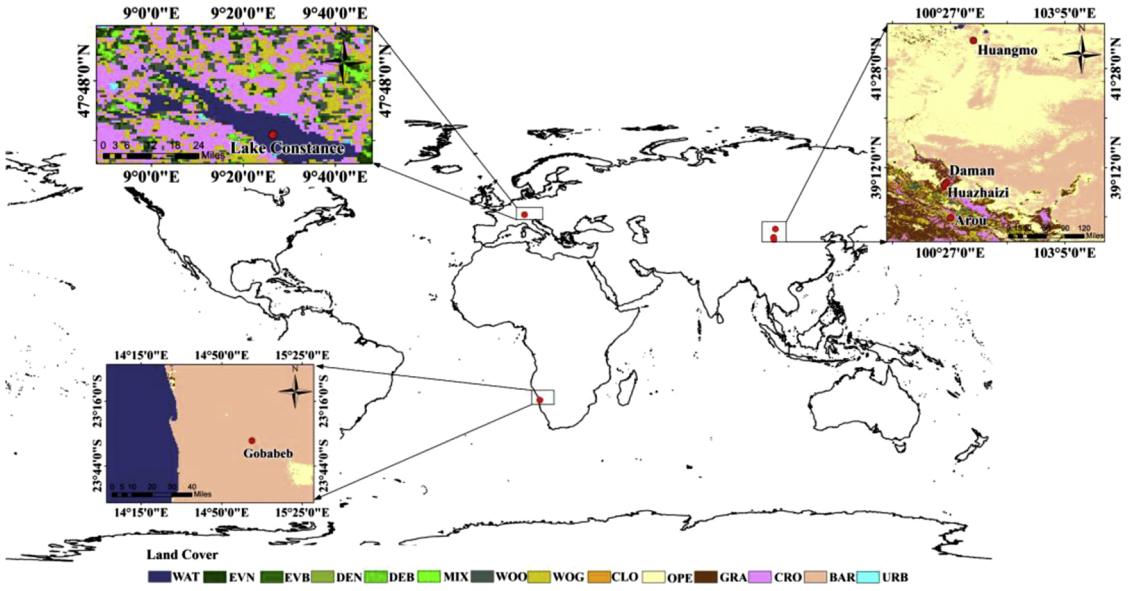

Fig. 1. The six validation sites and their land covers according to the 1-km AVHRR land cover classification map (Hansen et al., 1998): WAT – water; EVN – evergreen needleleaf forest; EVB – evergreen broadleaf forest; DEN – deciduous needleleaf forest; DEB - deciduous broadleaf forest; MIX – mixed forest; WOO – woodland; WOG – wooded grassland; CLO – closed shrubland; OPE – open shrubland; GRA – grassland; CRO – cropland; BAR – bare ground; and URB – urban and built.

actual situations, it is necessary to validate retrieved LST against *in-situ* LST (Yu et al., 2012; Duan et al., 2018). We collected *in-situ* measurements from six global ground sites with diverse underlying surfaces and climatic conditions (Table 2 and Fig. 1). Four of these sites, including Arou, Daman, Huazhaizi and Huangmo, are located in the Heihe River Basin (HRB) in northwest China and are part of the Heihe Watershed Applied Telemetry Experimental Research (HiWATER). HiWATER is a world-class watershed observing system and has provided long-term high-quality ground measurements for the validation of satellite land surface products (Li et al., 2013c; Liu et al., 2011, 2018). Specifically, Arou is located in the upstream of the HRB, with an underlying surface of subalpine meadow at an elevation of 3033 m; Daman and Huazhaizi have elevations of 1500 – 1800 m and are located in the HRB midstream, representing cropland and desert steppe, respectively; Huangmo is located in the downstream, with an underlying surface of desert and an elevation of 1054 m. *In-situ* incoming and outgoing longwave radiances at these four sites were measured with Eppley PIR at Daman, Kipp & Zonen CNR1 at Huazhaizi and Huangmo, and Kipp & Zonen CNR4 at Arou. Although these instruments have different uncertainties (PIR's uncertainty in daily total: 5%; CNR1's uncertainty in daily total: 10 %; and CNR4's uncertainty in daily total: < 10 %), their measurements agree well in inter-comparisons, with average root mean squared errors (RMSE) for incoming and outgoing longwave radiances of 6.43 W m^{-2} and 3.16 W m^{-2}, respectively (Xu et al., 2013). The field of view (FOV) diameters of these radiometers range from 37 m to 90 m. Our previous research shows that these four sites generally have moderate to high spatial representativeness at the 1-km scale. Following Liang (2005), the broadband LSE needed to obtain LST from longwave *in-situ* radiance measurements was calculated from MODIS channel 29, 31 and 32 LSEs of the MYD21 product; more details are provided in Zhou et al. (2015).

Gobabeb, the fifth site, is located on the highly homogeneous Namib

gravel plains and has a hyper-arid desert climate. The site is highly stable in space and time, therefore, ideal for the long-term validation of satellite products (Hulley et al., 2009a, 2009b). The Heitronics KT15.85 IIP radiometer (spectral response range: 9.6–11.5 μm) is mounted to a tower at 25 m with a view angle of 32°. The uncertainty of the observed BT is about 0.3 K (Theocharous et al., 2019). Downwelling sky radiance is measured by a second KT15.85 IIP with a zenith angle of 53°. Assuming that the KT15.85 IIP's channel effective LSE at Gobabeb is 0.94 (Göttsche and Hulley, 2012), the measured ground surface BT was converted to *in-situ* LST (Göttsche et al., 2013).

Lake Constance is located between Germany, Switzerland and Austria. Since 2014, KT15.85 IIP radiometers have been installed on the car ferry 'Friedrichshafen' to measure lake water surface temperature (LWST). Between 03:41 UTC and 19:21 UTC the ferry crosses the lake up to 16 times per day. The one-way travel distance is about 13.4 km and the travel time is about 40 min. The KT15.85 IIP radiometer is mounted at a height of 8 m above the water surface and LWST is retrieved with an uncertainty of < 0.4 K. The *in-situ* LWST is obtained from measured BTs using the same approach as for Gobabeb except that for moderate winds the LSE of water under 55° view angle is about 0.973 (Masuda et al., 1988) and downwelling sky radiance is measured at the complementary angle (i.e. water is a specular reflector).

3. Methodology

3.1. Candidate LST algorithms and their training

Based on our past experience in developing algorithms for the GLASS LST product (Zhou et al., 2019), the same 17 SWAs were selected as candidate algorithms for SLSTR. Some of these SWAs were also examined in the development of LST algorithms for NPOESS VIIRS (Yu et al., 2005, 2008). Although the formulas of these 17 SWAs are provided in Zhou et al. (2019), we list them in Tables 3 and 4 for the readers' convenience. Table 3 shows the SWAs requiring BTs and LSEs in the 11 μm and 12 μm channels, while Table 4 shows the SWAs that additionally require CWVC. Furthermore, BL1995 makes explicit use of view zenith angle (VZA).

MODTRAN 5 (Berk et al., 2005) was employed to conduct the forward atmospheric radiative transfer simulations for the 549 global atmospheric profiles contained in GAPD. The simulation scheme was similar to the one Zhou et al. (2019) used for developing the GLASS LST algorithms, except that the scheme needed to be adapted to the spectral response functions of SLSTR and to a possible inclusion of VZA as an additional parameter. The essential MODTRAN 5 parameters and their ranges are provided in Table 5; we used a parallel cluster to speed up the MODTRAN 5 simulations (Huang et al., 2016). The generated dataset consists of 3,162,240 samples, each of which contains simulated at-sensor brightness temperatures (BT_s), atmospheric parameters (atmospheric transmittance, up-welling radiance and down-welling radiance), and surface parameters (emissivity and LST). Gaussian-distributed random noise with noise equivalent delta temperatures between -0.05 K and 0.05 K (typical for channels S8 and S9) was added to the BTs to simulate real SLSTR observations; the obtained simulation dataset is hereinafter termed TRA-G (Table 1).

In order to obtain SWA results that are more accurate, the TRA-G dataset was divided into subsets characterizing different atmospheric conditions, daytime and nighttime, CWVC interval and VZA interval. The TRA-G data were divided as follows: (i) cold atmospheres (Cold-ATM: NSAT ≤ 280 K) and warm atmospheres (Warm-ATM: NSAT > 280 K); (ii) LST-NSAT differences between [-4 K, 20 K] or [-16 K, 4 K], representing daytime and nighttime, respectively; (iii) Cold-ATM samples were divided into three CWVC subranges (0.0 to 1.592 g cm^{-2} with increment 0.5 g cm^{-2}) and Warm-ATM samples into 13 CWVC subranges (0.0 to 6.0 g cm^{-2} with increment 0.5 g cm^{-2} and a subrange of [6.0–7.939 g·cm^{-2}]); (iv) 12 VZA values from 0 to 55° with an increment of 5°. Thus, for each VZA in Cold-ATM and Warm-ATM, the training sample size was 336 (7 LST-NSAT values × 48 LSEs) at daytime and 288 (6 LST-NSAT values × 48 LSEs) at nighttime times the number of respective atmospheric profiles. For each subset of atmospheric conditions and VZA, coefficient look-up tables (LUT) for each SWA were determined by regressing the respective formulae against the data.

3.2. LST retrieval from SLSTR data

LSE, CWVC and NSAT are the three essential SWA inputs required for retrieving LST from real SLSTR data. Considering the large possible spatial variation of LSE, it is necessary to determine SLSTR LSE on a per-pixel basis. All algorithms in Table 4 require CWVC as input parameters, and all SWAs require CWVC for selecting the coefficient LUT, since NSAT and CWVC were used for training the SWAs, they directly affect their coefficients.

LSE depends on land surface properties, such as land cover type, vegetation cover fraction, surface moisture content and roughness (Li et al., 2013b), it also depends on viewing angle (Sobrino, 2001; Sobrino et al., 2005). An alternative approach to determine LSE is to derive it from other available surface parameters, i.e. from land cover type and vegetation cover fraction (Peres and DaCamara, 2005). Here, we used the NDVI Thresholds Method (NDVI-THM) adapted to SLSTR data (Sobrino et al., 2016). NDVI-THM requires LSE estimates of the main land cover types, i.e. bare soil, vegetation, water and snow/ice. Here, we used emissivity spectra from the ASTER spectral library to obtain SLSTR LSE for each land cover type. The determined S8/S9 LSEs are 0.969/0.977 for bare soil, 0.982/0.984 for vegetation, 0.991/0.986 for

Table 3
The nine candidate SWAs that require BTs and LSEs as input.

No.	Name	Formula	Source
1	OV1992	$T_s = A_0 + A_1 T_{11} + A_2 (T_{11} - T_{12})$	Ottlé and Vidal-Madjar (1992)
2	FO1996	$T_s = A_0 + A_1 T_{11} + A_2 (T_{11} - T_{12}) + A_3 (T_{11} - T_{12})^2$	François and Ottlé (1996)
3	PR1984	$T_s = A_0 + A_1 T_{11} + A_2 (T_{11} - T_{12}) + A_3 T_{11} \varepsilon_{11} + A_4 (T_{11} - T_{12})(1 - \varepsilon_{11}) + A_5 T_{12} \Delta\varepsilon$	Price (1984)
4	UC1985	$T_s = A_0 + A_1 T_{11} + A_2 (T_{11} - T_{12}) + A_3 (1 - \varepsilon)$	Ulivieri and Cannizzaro (1985)
5	BL-WD	$T_s = A_0 + \left(A_1 + A_2 \frac{1-\varepsilon}{\varepsilon} + A_3 \frac{\Delta\varepsilon}{\varepsilon^2}\right)(T_{11} + T_{12}) + \left(A_4 + A_5 \frac{1-\varepsilon}{\varepsilon} + A_6 \frac{\Delta\varepsilon}{\varepsilon^2}\right)(T_{11} - T_{12})$	Becker and Li (1990) and Wan and Dozier (1996)
6	PP1991	$T_s = A_0 + A_1 \frac{T_{11} - T_0}{\varepsilon_{11}} + A_2 \frac{T_{12} - T_0}{\varepsilon_{12}} + A_3 \frac{1 - \varepsilon_{11}}{\varepsilon_{11}} + T_0$	Prata and Platt (1991)
7	VI1991	$T_s = A_0 + A_1 T_{11} + A_2 (T_{11} - T_{12}) + A_3 \frac{1-\varepsilon}{\varepsilon} + A_4 \frac{\Delta\varepsilon}{\varepsilon}$	Vidal (1991)
8	UL1994	$T_s = A_0 + A_1 T_{11} + A_2 (T_{11} - T_{12}) + A_3 (1 - \varepsilon) + A_4 \Delta\varepsilon$	Ulivieri et al. (1994)
9	WA2014	$T_s = A_0 + \left(A_1 + A_2 \frac{1-\varepsilon}{\varepsilon} + A_3 \frac{\Delta\varepsilon}{\varepsilon^2}\right)(T_{11} + T_{12}) + \left(A_4 + A_5 \frac{1-\varepsilon}{\varepsilon} + A_6 \frac{\Delta\varepsilon}{\varepsilon^2}\right)(T_{11} - T_{12}) + A_7 (T_{11} - T_{12})^2$	Wan (2014)

Note: subscripts 11 and 12 denote channels at approximately 11μm and 12μm, respectively, while T_{11} and T_{12} and ε_{11} and ε_{12} are their associated BTs and LSEs; $\varepsilon = (\varepsilon_{11} + \varepsilon_{12})/2$, $\Delta\varepsilon = (\varepsilon_{11} - \varepsilon_{12})$; the A_i are coefficients; T_0 in PP1991 is 273.15 K.

Table 4
The selected eight candidate SWAs that require BTs, LSEs and CWVC as input.

No.	Name	Formula	Source
1	FOW1996	$T_s = A_0 + (A_1 w + A_2 w^2 + A_3)T_{11} + (A_4 w + A_5 w^2 + A_6)T_{12} + A_7 w + A_8 w^2$	François and Ottle (1996)
2	SO1991	$T_s = A_0 + A_1 T_{11} + [A_2 w + A_3 + (A_4 w + A_5)(1-\varepsilon_{11}) + (A_6 w + A_7)\Delta\varepsilon](T_{11} - T_{12}) + \frac{1-\varepsilon_{11}}{\varepsilon_{11}} T_{11}[A_8 w + A_9 + (A_{10} w + A_{11})\Delta\varepsilon] - \frac{1-\varepsilon_{12}}{\varepsilon_{12}} T_{12}[A_{12} w + A_{13} + (A_{14} w + A_{15})\Delta\varepsilon]$	Sobrino et al. (1991)
3	ULW1994	$T_s = A_0 + A_1 T_{11} + (A_2 w + A_3)(T_{11} - T_{12}) + (A_4 w + A_5)(1-\varepsilon) + (A_6 w + A_7)\Delta\varepsilon$	Ulivieri et al. (1994)
4	CO1994	$T_s = A_0 + A_1 T_{11} + A_2(T_{11} - T_{12}) + A_3(T_{11} - T_{12})^2 + [(A_4 w + A_5)T_{11} + (A_6 w + A_7)](1-\varepsilon) - [(A_8 w + A_9)T_{11} + (A_{10} w + A_{11})]\Delta\varepsilon$	Coll et al. (1994)
5	SR2000	$T_s = A_0 + A_1 T_{11} + A_2(T_{11} - T_{12}) + A_3(T_{11} - T_{12})^2 + (A_4 w + A_5)(1-\varepsilon) - (A_6 w + A_7)\Delta\varepsilon$	Sobrino and Raissouni (2000)
6	MT2002	$T_s = A_0 + A_1 T_{11} + A_2(T_{11} - T_{12}) + A_3(T_{11} - T_{12})^2 + (A_4 w + A_5)(1-\varepsilon)$	Ma and Tsukamoto (2002)
7	BL1995	$T_s = A_0 + A_1 w + [A_2 + (A_3 w \cos\theta + A_4)(1-\varepsilon_{11}) - (A_5 w + A_6)\Delta\varepsilon](T_{11} + T_{12}) + [A_7 + A_8 w + (A_9 + A_{10} w)(1-\varepsilon_{11}) - (A_{11} w + A_{12})\Delta\varepsilon](T_{11} - T_{12})$	Becker and Li (1995)
8	GA2008	$T_s = A_0 + A_1 T_{11} + A_2(T_{11} - T_{12}) + A_3(T_{11} - T_{12})^2 + (A_4 + A_5 w + A_6 w^2)(1-\varepsilon) + (A_7 + A_8 w)\Delta\varepsilon$	Galve et al. (2008)

Note: w is CWVC and θ is VZA.

Table 5
Essential parameters and their ranges used for generating the TRA-G dataset.

Parameter	Range	Remark
LST	NSAT-16 K to NSAT + 20 K	Increment: 4 K
LSE in S8	0.667 − 0.995	48 materials
LSE in S9	0.656 − 0.991	48 materials
VZA	0 − 55°	Increment: 5°

Note: (i) Near Surface Air Temperature (NSAT) is provided in the atmospheric profiles and (ii) emissivity spectra of the 48 materials were obtained from the ASTER spectral library and convolved with the spectral response functions of channels S8 and S9 (Baldridge et al., 2009).

water, and 0.992/0.981 for snow and ice.

CWVC and NSAT values were extracted from the global ERA5 hourly data distributed by the Copernicus Climate Change Service (C3S) (https://cds.climate.copernicus.eu/). Both datasets are provided every hour and have a spatial resolution of 0.25° × 0.25°. Using linear interpolation, the ERA5 CWVC and NSAT values were temporally and spatially interpolated to estimate the CWVC and NSAT at each SLSTR pixel.

3.3. Evaluation of the SWAs

In order to obtain SWAs with low sensitivity to input parameters and a high retrieval accuracy, after a preliminary analysis of their training accuracies the algorithms were evaluated in three stages (Fig. 2). Stage I consists of an analysis of the algorithms' sensitivity to possible uncertainties in CWVC and LSE values provided by TRA-G. A sensitivity analysis for NSAT was not performed since it was only subdivided into two subranges. Instead of using the mathematical derivative approach to examine LST uncertainties due to all possible atmospheric parameters (Yu et al., 2008; Zhou et al., 2012), here we adopted the random noise approach also utilized by Zhou et al. (2019). Random uncertainties in CWVC and S8/S9 LSE at four levels were considered: (i) level 1: maximum $|\Delta w| \le 1.0\ \mathrm{g\,cm^{-2}}$, $|\Delta\varepsilon_{11}| \le 0.02$ and $|\Delta\varepsilon_{12}| \le 0.02$; (ii) level 2: maximum $|\Delta w| \le 1.0\ \mathrm{g\,cm^{-2}}$, $|\Delta\varepsilon_{11}| \le 0.04$ and $|\Delta\varepsilon_{12}| \le 0.04$; (iii) level 3: maximum $|\Delta w| \le 2.0\ \mathrm{g\,cm^{-2}}$, $|\Delta\varepsilon_{11}| \le 0.02$ and $|\Delta\varepsilon_{12}| \le 0.02$; and (iv) level 4: maximum $|\Delta w| \le 2.0\ \mathrm{g\,cm^{-2}}$, $|\Delta\varepsilon_{11}| \le 0.04$ and $|\Delta\varepsilon_{12}| \le 0.04$. At each level, the mean bias error (MBE) and RMSE of the LST estimates were calculated with the LST value provided in the TRA-G dataset as the truth.

Stage II tests the performance of SWAs that have passed Stage I. Stage II evaluates the SWAs against three datasets obtained from ATP-S, ATP-T and ATP-A with forward simulations, hereafter termed VAL-S, VAL-T and VAL-A (Table 1). VAL-S and VAL-T were used to assess SWA performance at global scale, while VAL-A assesses an algorithm's performance for extremely dry atmospheres. Details about the forward simulation procedure are provided in Zhou et al. (2019). Using simulation datasets allows a globally more representative algorithm assessment than with *in-situ* LSTs, since the latter are generally spatially sparse and not globally representative (Zhou et al., 2015).

Stage III validates the trained SWAs that passed Stage I and Stage II against *in-situ* LSTs from the six selected validation sites (see Section 2.3). To avoid possible cloud contamination, only pixel 1) containing the ground site and 2) for which the eight neighbors were flagged cloud-free were utilized. In order to remove some remaining outliers, which are generally caused by undetected clouds in the satellite data, we additionally applied 3σ (standard deviations) filtering to the matched-up satellite LST and *in-situ* LST data (Eq. (2)) (Göttsche et al., 2016; Pearson, 2002). For comparison, we also included the official SLSTR-LST product in the validation.

$$S = 1.4826 \cdot \mathrm{median}\{|x_k - x^*|\} \quad (2)$$

where the x_k are the differences between satellite LST and *in-situ* LST (i.e. the residuals) and x^* is their median. The matchups, which bias is greater than $x^* + 3S$ or less than x^*-3S, are removed.

4. Results

4.1. Algorithm training

The candidate algorithms were trained using least-squares optimization and standard error of estimation (SEE) was employed to quantify the achieved accuracy. The performance of the investigated 17 SLSTR SWAs was similar to that previously reported for NOAA AVHRR and Terra/Aqua MODIS (Zhou et al., 2019), which is unsurprising since the spectral response functions of the respective 11 μm/12 μm channels are similar. However, results show that six SWAs (i.e. UC1985, FOW1996, OV1992, FO1996, PP1991 and MT2002) yield higher SEEs than the other 11 SWAs (Fig.3). For a LST-NSAT range of [-4 K, 20 K], the SEEs of OV1992, FOW1996 and FO1996 all exceed 1.5 K and reach up to 4.0 K; the SEE ranges of PP1991, UC1985 and MT2002 are 0.58–3.77 K, 0.46–2.26 K and 0.45–2.14 K, respectively. The SEE values of UC1985 and MT2002 are lower than for FOW1996, OV1992, FO1996 and PP1991, but higher than for the other 11 SWAs. Similar training results are found for a LST- NSAT range of [-16 K, 4 K]. Therefore, the above six SWAs were excluded from the further examination.

For a LST- NSAT range of [− 4 K, 20 K] the SEEs of the other 11 SWAs are all lower than 2.2 K. For all CWVC and VZA subranges under Cold-ATM and for CWVC subranges lower than $2.5\ \mathrm{g\,cm^{-2}}$ under Warm-ATM, the SEEs of the 11 SWAs are lower than 0.8 K: this indicates quite high training accuracies of the 11 SWAs under dry and cold atmospheres. For Warm-ATM and CWVC exceeding $4\ \mathrm{g\,cm^{-2}}$, the

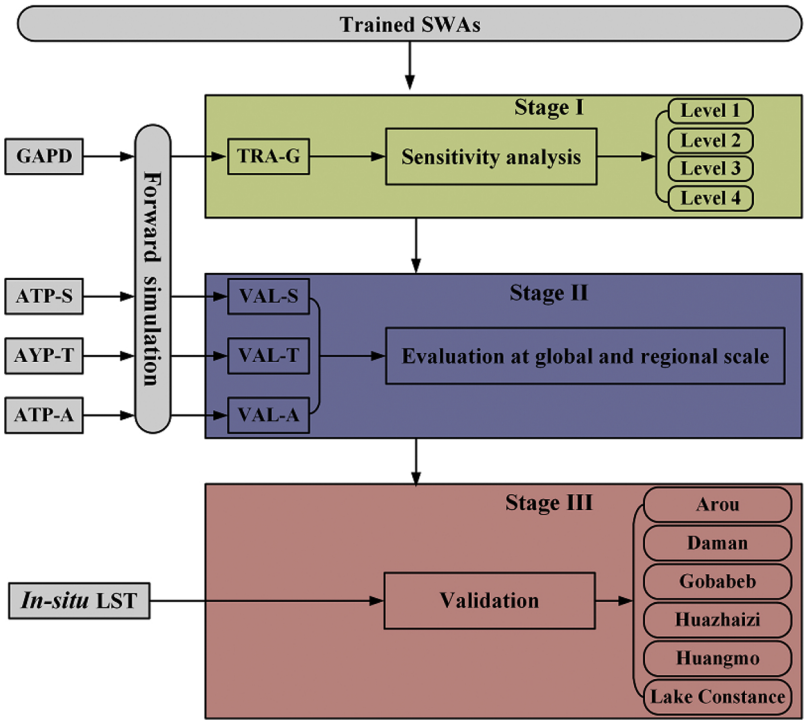

Fig. 2. Three-stage evaluation of trained SWAs.

SEE increases significantly especially when VZA is greater than 50°. Among the 11 SWAs, SO1991 and CO1994 have the best training accuracies, their SEE values are lower than 0.24 K and 0.27 K in Cold-ATM. BL-WD, WA2014 and BL1995 have slightly better training accuracies than PR1984, ULW1994, VI1991, SR2000, UL1994 and GA2008. Only the 11 SWAs with better training accuracies are studied further in Stage I.

4.2. Algorithm performance: stage I

Stage I investigates the sensitivity of the SWAs: Table 6 provides the determined MBE and RMSE values of the 11 algorithms. CO1994 and SO1991 exhibited a high sensitivity to input uncertainty, while the other nine SWAs had considerably lower MBE and RMSE of LST, with RMSEs lower than 1.0 K for level 1 and less than 1.4 K for level 4. Furthermore, Table 6 indicates that the nine better performing SWAs slightly underestimate LST. Based on these findings, CO1994 and SO1991 are not further investigated here.

4.3. Algorithm performance: stage II

Stage II examines the performance of the LST algorithms against the simulation datasets VAL-S, VAL-T and VAL-A. Table 7 shows the MBE and RMSE values of the nine SWAs that passed Stage I. For VAL-S and VAL-T, it can be seen that BL-WD, VI1991 and WA2014 slightly overestimate LST, whereas the other six SWAs exhibit negligible systematic LST errors. The RMSE ranges of the nine SWAs are 0.64 – 0.75 K and 0.77 – 0.87 K for VAL-S and VAL-T, respectively. These results demonstrate that the algorithms perform well under globally representative atmospheric conditions.

When evaluated against simulation data set VAL-A, BL-WD, VI1991, BL1995 and WA2014 show negligible systematic LST errors, while the other five SWAs (i.e. PR1984, UL1994, ULW1994, SR2000 and GA2008) slightly underestimate LST. However, all nine SWAs have RMSEs of less than 1 K. Overall, BL-WD and WA2014 perform slightly better than the other seven SWAs, while the accuracies of SR2000 and GA2008 are slightly lower.

Since the atmospheric profiles in ATP-S and ATP-T are globally distributed, we obtained RMSEs for each SWA per land cover type. Land cover types are mainly based on the global AVHRR land cover classification (Hansen et al., 1998). Following the global soil classification approach of the Food and Agriculture Organization of the United Nations (http://www.fao.org/soils-portal/en/), pixels flagged as bare ground were further classified into four sub types (i.e. ICE, ROC, SHI and BAR). Fig.4 shows the RMSE values of the nine SWAs for each land cover type. For VAL-S and for all SWAs and land cover types but ROC, RMSE values are lower than 0.9 K. Similarly, for VAL-T all RMSE values are generally lower than 0.9 K but for land cover type BAR. No obvious dependence of retrieval accuracy on LSE or land cover type has been found. Generally, for most land cover types the BL-WD algorithm performs best, i.e. it has the lowest RMSE. In most cases, the SR2000, BL1995 and GA2008 have slightly higher RMSEs than the other SWAs.

In general, the accuracy of the nine SWAs decreases with increasing CWVC (Fig.5), thereby demonstrating that the atmospheric influence is not totally compensated. The determined RMSEs are quite similar, which suggests that GAPD is suitable for training SWAs for LST retrieval from SLSTR data.

4.4. Algorithm performance: stage III

The nine SWAs retained after Stage II were applied to estimate LST from Sentinel-3A SLSTR data. LST maps retrieved with BL-WD over the six validation sites are shown in Fig. 6. The sites are categorized according to their (predominant) land cover type into vegetation, barren surface and water sites.

4.4.1. Vegetation sites

Arou and Daman are vegetation sites and Table 8 shows their corresponding validation results (i.e. MBE, RMSE, sample size N and coefficient of determination R^2). For Arou, 121 matchups between satellite LST and *in-situ* LST were obtained from January 1th, 2017 to December 31th, 2017. The nine investigated SWAs had similar accuracies with RMSEs ranging from 2.73 K (PR1984) to 3.10 K (VI1991) (mean: 2.88 K; standard deviation (STD): 0.10 K). Interestingly, the

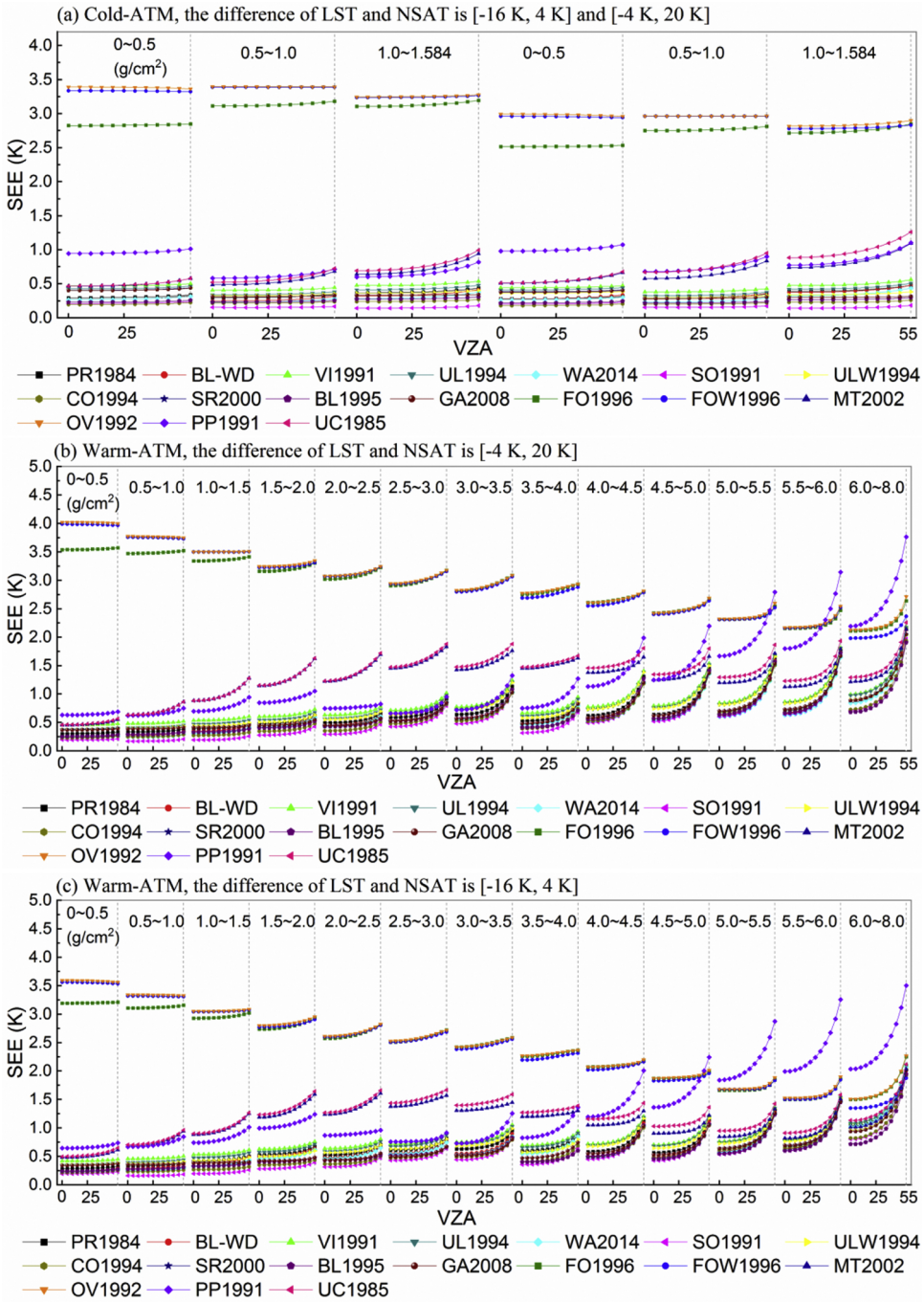

Fig. 3. The SEEs of the trained 17 SWAs.

SWAs with the best and lowest accuracies are not the same as in Stage II. Furthermore, all SWAs overestimate LST, with MBEs ranging from 1.91 K to 2.46 K. LST is greatly overestimated during Summer (Fig. 7), which may be explained by a stronger atmospheric influence on TIR satellite observations due to generally warmer and more humid atmospheres. In comparison, the MBE and RMSE of the SLSTR product for Arou are 3.63 K and 4.18 K, respectively (Table 8 and Fig. 7a).

The performance of the nine SWAs over Daman is similar to that over Arou (Table 8), but with higher RMSEs from 3.38 K (PR1984) to 3.66 K (VI1991), a mean of 3.49 K and a STD of 0.07 K. LST is primarily overestimated during Summer and MBEs range from 2.27 K to 2.76 K (Table 8 and Fig. 7b). In contrast, the SLSTR LST product generally overestimates LST with a MBE of 3.95 K and a RMSE of 4.51 K (Fig. 7b).

4.4.2. Barren sites

The three sites Huazhaizi, Huangmo and Gobabeb are categorized as barren surface and their validation results are provided in Table 9. For Huazhaizi and Huangmo, the nine SWAs yield RMSEs between 2.82 K and 3.23 K with corresponding means of 3.01 K (STD: 0.01 K) and 3.15 K (STD: 0.05 K), respectively. In contrast, the RMSE of the SLSTR LST product is 5.56 K and 4.70 K for Huazhaizi and Huangmo, respectively. For both sites, the nine SWAs and the SLSTR product overestimate LST.

In contrast, considerably better validation results are obtained for the Gobabeb site. Because the area within 1 km around the validation station is more heterogeneous in terms of soil type and topography, pixel should be extracted at the highly homogeneous part of the gravel plains (Göttsche et al., 2013). Therefore, the location chosen to extract

Table 6
MBE and RMSE of 11 SWAs investigated at Stage 1 for four uncertainties levels shown in Section 3.3.

SWA	Level 1 (K)		Level 2 (K)		Level 3 (K)		Level 4 (K)	
	MBE	RMSE	MBE	RMSE	MBE	RMSE	MBE	RMSE
PR1984	−0.07	0.89	−0.08	1.16	−0.15	1.10	−0.16	1.33
BL-WD	−0.08	0.87	−0.08	1.15	−0.16	1.10	−0.16	1.32
VI1991	−0.07	0.95	−0.07	1.21	−0.14	1.13	−0.15	1.35
UL1994	−0.07	0.92	−0.07	1.17	−0.15	1.10	−0.15	1.32
WA2014	−0.06	0.87	−0.07	1.16	−0.15	1.11	−0.15	1.35
SO1991	3.32	8.30	3.32	8.39	3.19	8.53	3.19	8.61
ULW1994	−0.07	0.89	−0.07	1.15	−0.16	1.10	−0.16	1.32
CO1994	−1.39	4.32	−1.38	4.39	−1.46	4.39	−1.45	4.46
SR2000	−0.06	0.88	−0.07	1.16	−0.16	1.13	−0.17	1.36
BL1995	−0.08	0.85	−0.09	1.15	−0.17	1.10	−0.18	1.34
GA2008	−0.06	0.88	−0.06	1.17	−0.15	1.16	−0.16	1.39

Table 7
MBE and RMSE of nine SWAs investigated at Stage II for three simulation data sets; N is the number of samples in a data set.

SWA	VAL-S (K) (N = 47,610)		VAL-T(K) (N = 5060)		VAL-A (K) (N = 160)	
	MBE	RMSE	MBE	RMSE	MBE	RMSE
PR1984	0.01	0.68	−0.02	0.82	−0.12	0.90
BL-WD	0.16	0.64	0.12	0.77	−0.05	0.76
VI1991	0.23	0.72	0.20	0.84	0.0	0.81
UL1994	0.02	0.70	−0.02	0.83	−0.19	0.85
WA2014	0.17	0.65	0.12	0.77	−0.01	0.78
ULW1994	0.04	0.69	−0.03	0.82	−0.21	0.78
SR2000	0.07	0.74	−0.01	0.87	−0.14	0.96
BL1995	0.07	0.71	0.0	0.83	−0.07	0.82
GA2008	0.08	0.75	−0.01	0.87	−0.14	0.96

the satellite pixels is: 23.55 °S, 15.06 °E. As described in Section 3.3, we additionally applied 3σ filtering to remove some outliers. The LST MBEs and RMSEs retrieved with the nine SWAs range from -0.30 K to -0.16 K and from 1.57 K to 1.62 K, respectively, and have similar performance (0.04 K STD of MBE and 0.02 K STD of RMSE). Furthermore, the performances of the SWAs at Gobabeb resemble those found in Stage II: BL-WD has the lowest RMSE (1.57 K), whereas SR2000 and GA2008 have the highest RMSEs (1.62 K and 1.61 K), although this difference is small. For Gobabeb, the SLSTR LST also exhibit considerably better accuracy than for the other two barren surface sites (RMSE of 2.36 K). However, the SLSTR LST product still significantly overestimates LST (MBE: 1.56 K), whereas the nine SWAs slightly underestimate LST (Table 9 and Fig. 8).

4.4.3. Water site

The validation results for Lake Constance are presented in Fig. 9 and Table 10. As described in Section 3.3, we applied the 3σ filtering to remove the outliers, which have not been removed by the cloud-screening, and four matchups were removed. From January 1th, 2018 to December 31th, 2018, 33 valid matchups between retrieved SLSTR LSTs and *in-situ* LWST were obtained. The MBEs and RMSEs of the nine SWAs range from -0.17 K to 0.31 K (mean value: -0.05 K; STD: 0.15 K) and 0.49 K to 0.61 K (mean value: 0.53 K; STD: 0.03 K), respectively, indicating that some SWAs underestimate LST slightly, but consistently. BL-WD, UL1994, ULW1994 and WA2014 have ignorable systematic error. The relative performance of the nine SWAs is similar to that obtained for the three simulation datasets (Stage II): BL-WD has better accuracy (i.e. lower RMSE) than most of the other SWAs. In contrast, the SLSTR product slightly overestimates LST (MBE of 0.36 K) and with a RMSE is 0.69 K.

5. Discussion

The training results and the three-stage evaluation of the SWAs indicate a generally good performance of the nine selected algorithms, which are also consistent with each other (Fig. 10). This finding is in agreement with the results previously reported by Yu et al. (2008) for VIIRS. Although the obtained MBE and RMSE values differ between validation sites, on a global scale the nine selected SWAs exhibit no significant biases, which is consistent with the results obtained for the simulation data sets VAL-S and VAL-T in Stage II. Furthermore, the evaluation against VAL-A, i.e. a regional simulation dataset for the Tibetan Plateau, also supports this finding. The SWAs validation results show that each algorithm performs slightly differently under different conditions. Therefore, multi-algorithm ensemble approaches, e.g. the Bayesian Model Averaging (BMA), which combines the estimates of different SWAs (Zhou et al., 2019), have the potential to obtain improved LST estimates. Therefore, each of the nine SWAs or their combination can be used for retrieving LST from Sentinel-3 SLSTR data.

The evaluation in stage III highlighted that SWA performance can differ considerably for the six validation sites. This can have several reasons, e.g. LST retrieval error and uncertainty in *in-situ* LST (Guillevic et al., 2014). For the dedicated LST validation site Gobabeb, all nine SWAs performed well. Gobabeb is a highly homogeneous desert site on the vast gravel plains of the Namib: thus, *in-situ* measurements are spatially representative from the meter to the km pixel scale. It is a 'gold standard reference' site for validating satellite LST products such as SEVIRI and SLSTR LSTs (Ghent et al., 2017). Gobabeb LST validation station employs accurate (RMSE of 0.3 K) and stable Heitronics KT15.85 IIP radiometers for obtaining *in-situ* LST (Theocharous et al., 2019). KT15.85 IIP radiometers have a single narrow TIR channel (9.6–11.5 μm) and a full view angle of 8.3°, which leads to directional measurements resembling those of satellite sensors. Representing a homogeneous water surface with a high and well-defined emissivity, Lake Constance offers even more ideal conditions than the gravel plains at Gobabeb. This explains why the results for these two sites agree best with those obtained for the simulation datasets in Stage II: both evaluations show that BL-WD and WA2014 generally perform well (the latter with slightly lower accuracy). Furthermore, these two algorithms also form the basis of the daily 1-km MODIS LST Collection 6 product (i.e. M*D11_L2).

Relatively larger MBEs and RMSEs are obtained for the other four sites (Arou, Daman, Huazhaizi and Huangmo). At these sites, the instruments for the *in-situ* radiance measurements are hemispherical broadband radiometers. While the broad FOV of these radiometers reduces the spatial scale miss-match between *in-situ* and satellite measurements, one should note that (i) hemispherical *in-situ* observations intrinsically differ from directional satellite observations (Li et al., 2019) and (ii) due to their large spectral range, broadband *in-situ* observations are more strongly affected by the intervening atmosphere. The validation results are also affected by differences in surface homogeneity, which may explain the slightly lower performance of the nine SWAs at Daman and Huangzhaizi. In particular at Daman the relatively low performance is thought to be due to a heterogeneous surface and to an insufficient mounting height of the four-component radiometer, resulting in spatially unrepresentative measurements. In contrast, an explanation for the lower performance observed at Huangmo is currently missing.

According to Eq. (1), the official SLSTR LST product depends on the input parameters vegetation type (biome), vegetation fraction and CWVC. The official SLSTR LST algorithm, which incorporates LSE into its coefficients via the biome, is less sensitive to LSE errors: this makes the algorithm independent of LSE accuracy and can yield more robust LST estimates when LSE is not well known (Liu et al., 2015; Yu et al., 2018). However, significant uncertainties may be introduced into such algorithms due to misclassification (Sobrino et al., 2016). In contrast, SWAs with an explicit use of LSE can accommodate within 'class

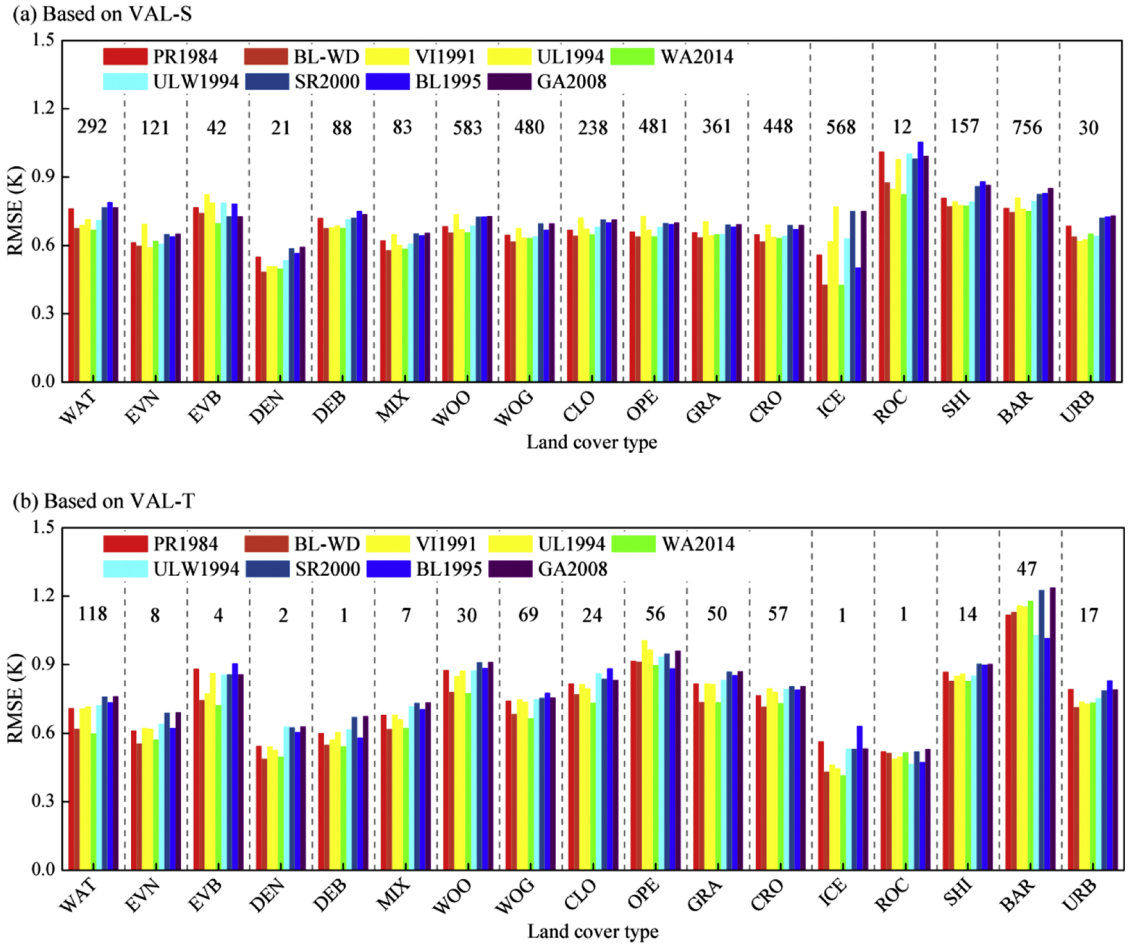

Fig. 4. RMSEs obtained with VAL-S and VAL-T for different land cover types. Above the bars, the number of available atmospheric profiles for each land cover type is provided. Land cover types: ICE – bare ground (ice); ROC – bare ground (Rock); and SHI – bare ground (Shifting sand); BAR – bare ground (other soil types); the other land cover types provided in Fig. 1.

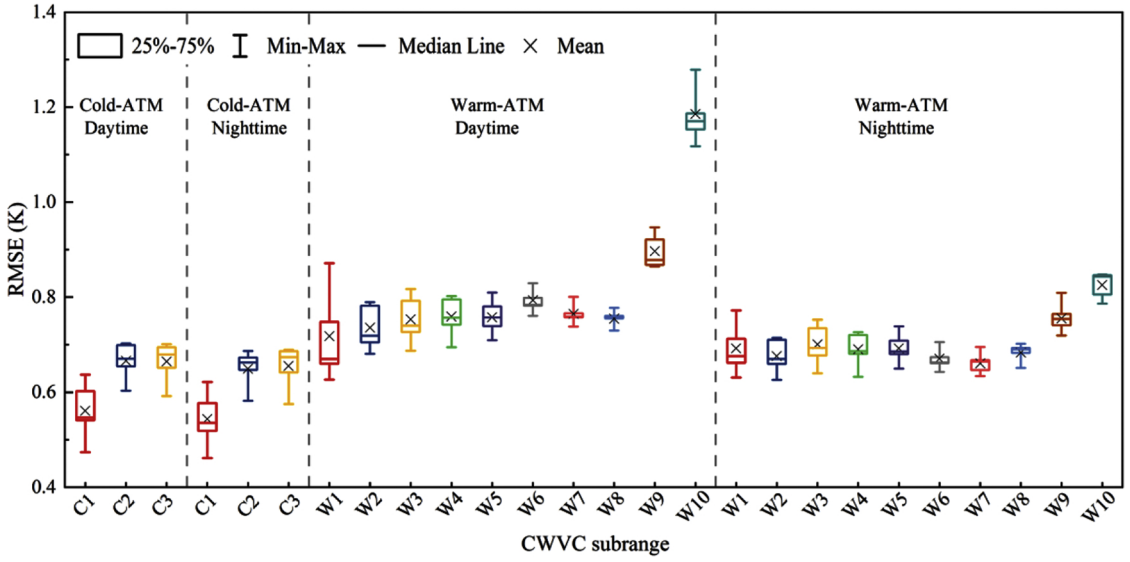

Fig. 5. RMSE values of the nine SWAs under different atmospheric conditions based on VAL-S for different CWVC subranges: C1 – CWVC∈[0.0-0.5 g·cm^{-2}]; C2 – CWVC∈[0.5-1.0 g·cm^{-2}]; C3 – CWVC∈[1.0-2.6 g·cm^{-2}]; W1 – CWVC∈[0.0-0.5 g·cm^{-2}]; W2 – CWVC∈[0.5-1.0 g·cm^{-2}]; W3 – CWVC∈[1.0-1.5 g·cm^{-2}]; W4 – CWVC∈[1.5-2.0 g·cm^{-2}]; W5 – CWVC∈[2.0-2.5 g·cm^{-2}]; W6 – CWVC∈[2.5-3.0 g·cm^{-2}]; W7 – CWVC∈[3.0-3.5 g·cm^{-2}]; W8 – CWVC∈[3.5-4.0 g·cm^{-2}]; W9 – CWVC∈[4.0-4.5 g·cm^{-2}]; W10 – CWVC∈[4.5-5.0 g·cm^{-2}].

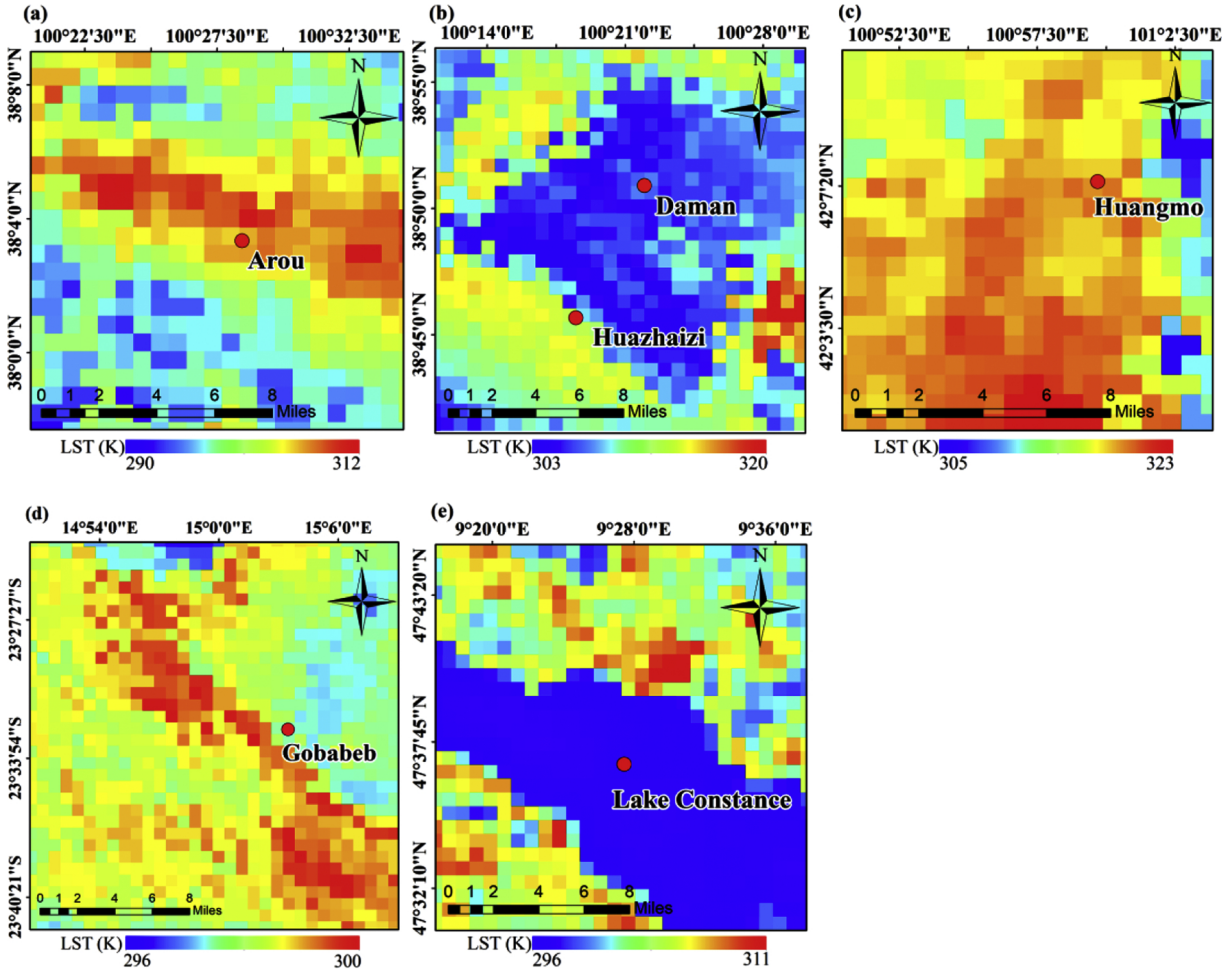

Fig. 6. LST maps retrieved with BL-WD over six validation sites: (a) Arou, July 19th 2017; (b) Daman and Huazhaizi, June 12th 2017; (c) Huangmo, June 10th 2017; (d) Gobabeb, June 22th 2018; and (e) Lake Constance, July 18th 2018.

variability' (Yu et al., 2005) and can easily integrate improved LSE data: this allows to directly convert improvements in input emissivity into improved LST retrievals (Hulley et al., 2009a, 2015; Sobrino et al., 2016). An inspection of the six sites confirms that the prescribed biome types are generally correct (for Huazhaizi, Huangmo, Gobabeb and Lake Constance). Furthermore, the time series of vegetation fraction describes realistic seasonal variations and there appears to be a linear relationship between CWVC and LST error; the latter is demonstrated for Gobabeb and Lake Constance in Fig. 11. For comparison, the results for BL-WD are also shown. They show that the SLSTR product generally overestimates LST and that LST error increases with CWVC. The positive linear dependence of the SLSTR product on CWVC suggests that its accuracy decreases for humid atmospheric conditions, while there is a weaker correlation between LST error estimated with BL-WD and CWVC.

As an input parameter of some LST algorithms, CWVC directly affects their accuracy. The trained SWAs require CWVC to select the retrieval coefficients. Besides utilizing publicly available CWVC products, some methods determine CWVC directly and quantitatively from split-window radiance measurements, e.g. the method refined by Li et al. (2003) (hereinafter referred to as Li2003). We used the Li2003 method to estimate CWVC from SLSTR data and then incorporated these estimates into SWAs. Since the Gobabeb site is highly homogeneous and well characterized and the validation station provides highly accurate

Table 8
LST validation results for nine SWAs and the SLSTR product at Arou and Daman.

SWA	Arou				Daman			
	MBE (K)	RMSE (K)	N	R^2	MBE (K)	RMSE (K)	N	R^2
PR1984	1.91	2.73	121	0.98	2.27	3.38	88	0.96
BL-WD	2.21	2.90	121	0.98	2.51	3.48	88	0.96
VI1991	2.46	3.10	121	0.98	2.76	3.66	88	0.97
UL1994	2.19	2.88	121	0.98	2.50	3.48	88	0.96
WA2014	2.16	2.86	121	0.98	2.48	3.47	88	0.96
ULW1994	2.12	2.86	121	0.98	2.43	3.45	88	0.96
SR2000	2.07	2.86	121	0.98	2.47	3.51	88	0.96
BL1995	2.10	2.87	121	0.98	2.31	3.45	88	0.96
GA2008	2.07	2.86	121	0.98	2.47	3.52	88	0.96
SLSTR product	3.63	4.18	121	0.97	3.95	4.51	88	0.97

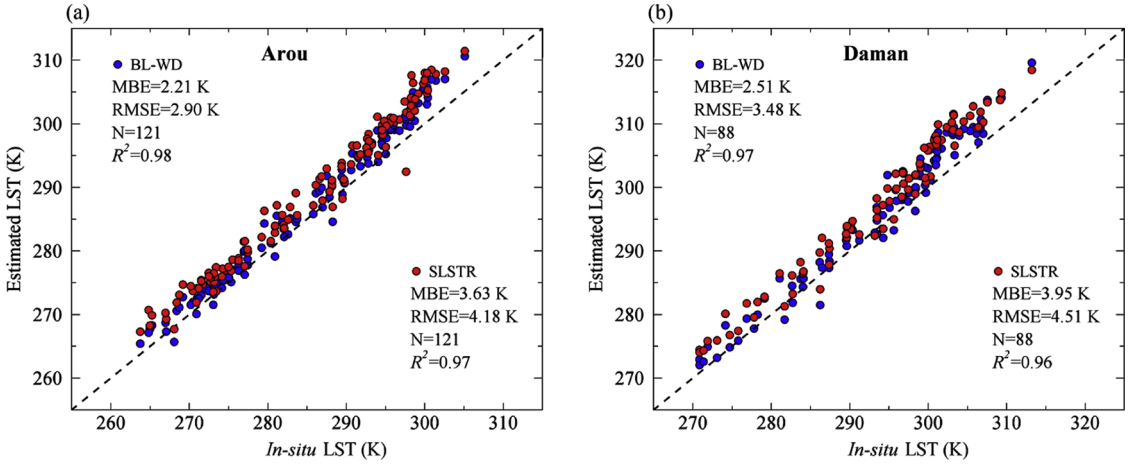

Fig. 7. LST estimated with BL-WD and the SLSTR LST product versus *in-situ* LST for Arou (a) and Daman (b). 13 matchups are filtered out by the additional cloud screening for Arou and 2 matchups for Daman.

Table 9
LST validation results for nine SWAs and the SLSTR product at Huazhaizi, Huangmo and Gobabeb.

SWA	Huazhaizi				Huangmo				Gobabeb			
	MBE (K)	RMSE (K)	N	R^2	MBE (K)	RMSE (K)	N	R^2	MBE (K)	RMSE (K)	N	R^2
PR1984	1.54	2.94	72	0.98	1.62	3.12	123	0.99	−0.30	1.59	119	0.97
BL-WD	1.74	2.95	72	0.98	1.88	3.12	123	0.99	−0.21	1.57	119	0.97
VI1991	2.08	3.20	72	0.98	2.08	3.23	123	0.99	−0.16	1.58	119	0.97
UL1994	1.81	3.04	72	0.98	1.93	3.18	123	0.99	−0.23	1.58	119	0.97
WA2014	1.58	2.82	72	0.98	1.78	3.06	123	0.99	−0.24	1.61	119	0.96
ULW1994	1.73	3.04	72	0.98	1.81	3.17	123	0.99	−0.25	1.59	119	0.97
SR2000	1.74	3.04	72	0.98	1.76	3.17	123	0.99	−0.20	1.62	119	0.96
BL1995	1.57	3.02	72	0.98	1.59	3.17	123	0.99	−0.29	1.59	119	0.96
GA2008	1.73	3.04	72	0.98	1.76	3.17	123	0.99	−0.20	1.61	119	0.96
SLSTR product	5.14	5.56	72	0.98	4.26	4.70	123	0.99	1.56	2.36	119	0.95

Note: 15 matchups are filtered out by the additional cloud screening for Huazhaizi.

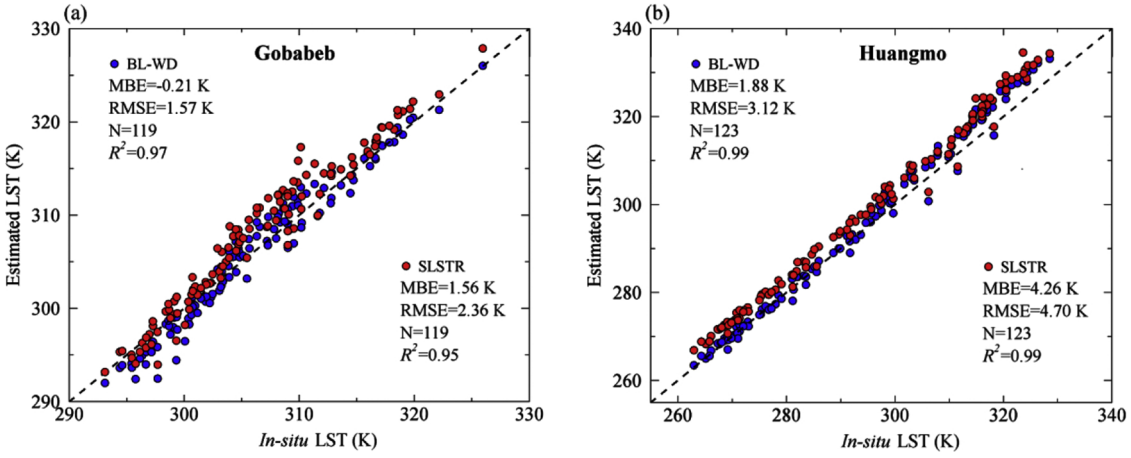

Fig. 8. LST estimated with BL-WD and the SLSTR LST product versus *in-situ* LST for Gobabeb (a) and Huangmo (b). 23 matchups are filtered out by the additional cloud screening for Gobabeb and 10 matchups for Huangmo.

and representative *in-situ* LST, we focused on this site for a more detailed validation. We compared Li2003-CWVC with ERA5-CWVC, for which some interesting results were found: first, Li2003-CWVC and ERA5-CWVC are relatively close when ERA5-CWVC is high (ERA5-CWVC > 1 g cm^{-2}), with a mean deviation between ERA5 and Li2003 of 0.10 g cm^{-2}. Second, when ERA5-CWVC < 1 g cm^{-2}, Li2003-CWVC is significantly higher than ERA5-CWVC, and the corresponding mean deviation is 0.83 g cm^{-2}. Third, Li2003-CWVC occasionally exhibits sudden changes. We also found that ERA5-CWVC has typical intra-annual variation, which seems that it agrees well with the climate at the Gobabeb site. In contrast, Li2003-CWVC does not accurately reflect the intra-annual weather characteristics at Gobabeb, especially under very dry atmospheres.

We then validated LST estimates based on Li2003-CWVC (hereinafter termed Li2003-LST) and LST estimates based on ERA5-CWVC (hereinafter termed ERA5-LST) against *in-situ* LST. The RMSE of Li2003-LST ranges from 1.80 K to 1.99 K, while the RMSE of ERA5-LST ranges from 1.44 K to 1.49 K. Overall, the accuracy of LST calculated

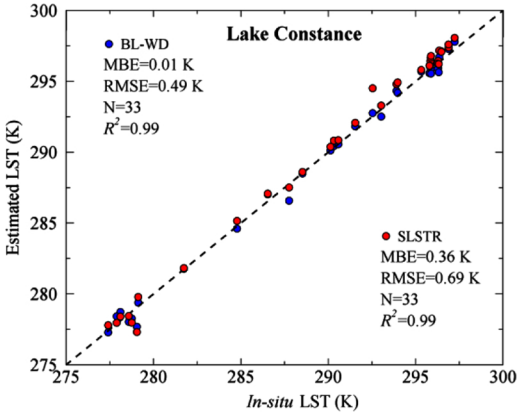

Fig. 9. LST estimated with BL-WD and the SLSTR LST product versus *in-situ* LWST for Lake Constance. 6 matchups are filtered out by the additional cloud screening for Lake Constance.

Table 10
LST validation results for nine SWAs and the SLSTR product at Lake Constance.

SWA	MBE (K)	RMSE (K)	N	R^2
PR1984	−0.17	0.51	33	0.99
BL-WD	0.01	0.49	33	0.99
VI1991	0.31	0.61	33	0.99
UL1994	−0.02	0.53	33	0.99
WA2014	−0.04	0.52	33	0.99
ULW1994	−0.03	0.52	33	0.99
SR2000	−0.17	0.55	33	0.99
BL1995	−0.15	0.52	33	0.99
GA2008	−0.17	0.55	33	0.99
SLSTR product	0.36	0.69	33	0.99

using ERA5-CWVC is considerably higher. In summary, for wet atmospheres, Li2003 appears to be a reliable method for estimating CWVC directly from satellite data. For dry atmospheres, using the ERA5 CWVC product is more accurate and a convenient strategy for estimating LST.

6. Conclusions

Sentinel-3 SLSTR is operated within the European Union's Earth Observation Programme 'Copernicus' and provides global and high quality thermal infrared remote sensing data. The official LST product retrieved from SLSTR implicitly relies on LSE and is an important and freely available source of satellite LST data. The main objective of this study is to develop alternative SLSTR LST retrieval algorithms, which use LSE explicitly rather than implicitly. Therefore, seventeen candidate split-window algorithms (SWAs) were selected and trained with a global simulation dataset. The training and sensitivity analysis showed that nine of the seventeen SWAs had both good training accuracy and low sensitivity. These nine SWAs were evaluated in three stages and their results compared with the official SLSTR LST product. The nine SWAs were evaluated against two global simulation datasets (i.e. VAL-S and VAL-T) and a regional simulation dataset (i.e. VAL-A): all nine algorithms had similar accuracy, negligible systematic error and RMSEs of less than 1.0 K. Therefore, it is concluded that the nine SWAs perform well on the global scale, including under extremely dry atmospheric conditions. The algorithms BL-WD and WA2014 had the highest relative accuracy of the nine SWAs.

The validation against *in-situ* LSTs from six globally distributed sites confirmed the similar accuracy of the nine SWAs. For the validation stations Gobabeb (desert, gravel plain) and Lake Constance (water), which are equipped with highly stable precision thermal infrared radiometers, the range of RMSEs for the nine SWAs are 1.57–1.62 K and 0.49 − 0.61 K, respectively. All nine SWAs underestimated LST at Gobabeb. No systematic errors of BL−WD and WA2014 were observed at Lake Constance. In contrast, RMSEs of 2.73–3.66 K and considerably overestimated LSTs were observed at the four sites equipped with hemispherical broadband radiometers. While the broad FOV of these radiometers reduces the spatial scale miss-match between *in-situ* and satellite measurements, hemispherical broadband *in-situ* observations intrinsically differ from directional satellite observations and are more affected by the intervening atmosphere. Additionally, the validation results reflect the different surface homogeneity of the sites. The results further indicate that the official SLSTR product has lower accuracy than the nine investigated SWAs, especially when compared to BL−WD and WA2014.

The investigated SWAs can directly serve as alternative retrieval algorithms for SLSTR LST. Since the LST retrieval algorithm underlying BL-WD and WA2014 is also the basis of the daily 1-km MODIS LST Collection 6 product (M*D11_L2), these two SLSTR SWAs may reduce the bias between MODIS and SLSTR LSTs. Finally, the investigated SWAs and findings presented in this study are a contribution to the continued evaluation of the operational SLSTR LST product, thereby increasing its maturity. The program and retrieval coefficients of SWAs can be requested via e-mail to jzhou233@uestc.edu.cn.

CRediT authorship contribution statement

Jiajia Yang: Methodology, Formal analysis, Software, Writing -

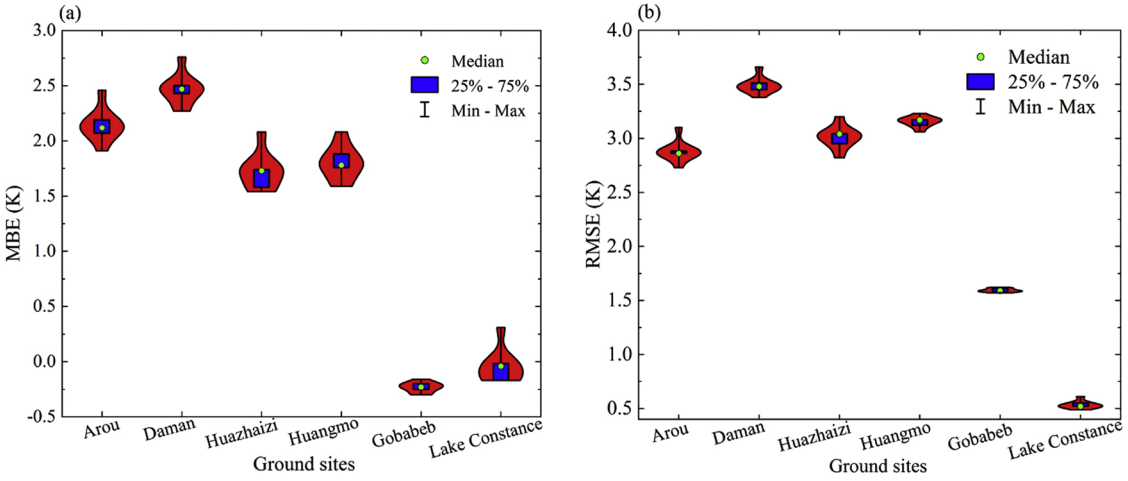

Fig. 10. Violin plots for MBE (a) and RMSE (b) of the nine selected SWAs at the six sites. Wider red areas indicate that more SWAs are in the respective range, and vice versa (For interpretation of the references to colour in this figure legend, the reader is referred to the web version of this article).

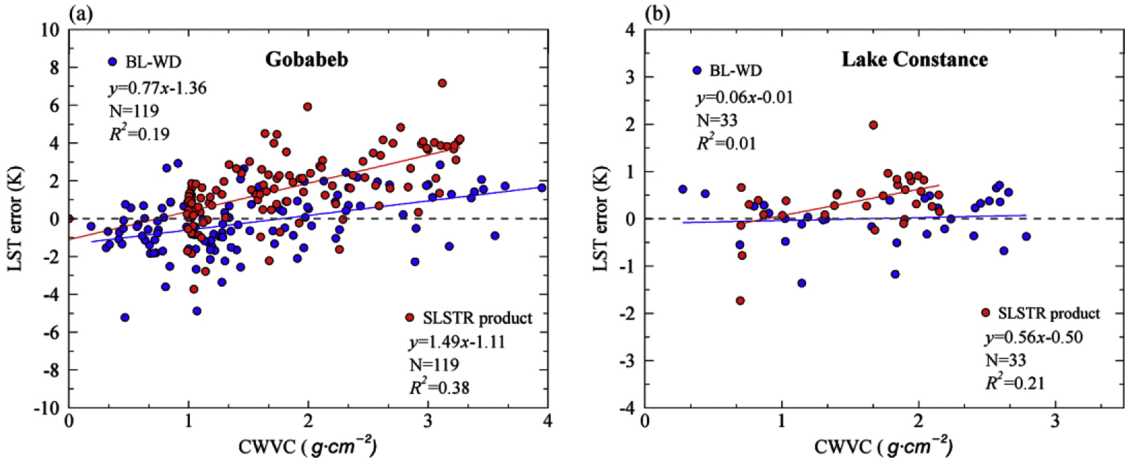

Fig. 11. Estimates of LST error versus CWVC for Gobabeb (a) and Lake Constance (b).

original draft, Validation. **Ji Zhou:** Conceptualization, Methodology, Formal analysis, Data curation, Writing - review & editing. **Frank-Michael Göttsche:** Resources, Formal analysis, Writing - review & editing. **Zhiyong Long:** Formal analysis, Writing - review & editing. **Jin Ma:** Software, Validation. **Ren Luo:** Software, Validation.

Declaration of Competing interest

The authors declare that they have no known competing financial interests or personal relationships that could have appeared to influence the work reported in this paper.

Acknowledgements

This work was supported by the National Natural Science Foundation of China (grant number: 41531174 and 41871241) and by the Fundamental Research Funds for the Central Universities of China under grant ZYGX2019J069. The authors would like to thank the National Tibet PlateauScientific Data Center (http://data.tpdc.ac.cn) for providing the *In-situ* validation data for the four sites in Heihe, and Karlsruhe Institute of Technology (KIT), Germany, for supporting the maintenance and operation of the *in-situ* LST validation stations at Gobabeb and Lake Constance. The ERA5 data were provided by the Copernicus Climate Change Service (C3S) (https://cds.climate.copernicus.eu/). The brightness temperature data and official LST product of Sentinel-3A SLSTR were provided by Copernicus Open Access Hub (https://scihub.copernicus.eu/). We thank the Bodensee-Schiffsbetriebe (BSB) GmbH, Germany, for their generous and continued support of the measurements on-board the ferry Friedrichshafen. We would also like to thank Wang Yujia from University of Electronic Science and Technology of China for her contribution in the forward simulation.

References

Baldridge, A.M., Hook, S.J., Grove, C.I., Rivera, G., 2009. The ASTER spectral library version 2.0. Remote Sens. Environ. 113, 711–715.
Becker, F., Li, Z.-L., 1990. Towards a local split window method over land surfaces. Int. J. Remote Sens. 11, 369–393.
Becker, F., Li, Z.-L., 1995. Surface temperature and emissivity at various scales: definition, measurement and related problems. Remote. Sens. Rev. 12, 225–253.
Berk, A., Anderson, G.P., Acharya, P.K., Bernstein, L.S., Muratov, L., Lee, J., Fox, M., Adler-Golden, S.M., Chetwynd, J.H., Hoke, M.L., Lockwood, R.B., Gardner, J.A., Cooley, T.W., Borel, C.C., Lewis, P.E., 2005. MODTRAN 5: A Reformulated Atmospheric Band Model With Auxiliary Species and Practical Multiple Scattering Options: Update. pp. 662–667.
Borbas, E.E., Seemann, S.W., Huang, H.-L., Li, J., Menzel, W.P., 2005. Global profile training database for satellite regression retrievals with estimates of skin temperature and emissivity. In: Proc. XIV Int. ATOVS Study Conf. Beijing, China. pp. 763–770.
Chatterjee, R.S., Singh, N., Thapa, S., Sharma, D., Kumar, D., 2017. Retrieval of land surface temperature (LST) from landsat TM6 and TIRS data by single channel radiative transfer algorithm using satellite and ground-based inputs. Int. J. Appl. Earth Obs. Geoinf. 58, 264–277.
Coll, C., Caselles, V., Sobrino, J.A., Valor, E., 1994. On the atmospheric dependence of the split-window equation for land surface temperature. Int. J. Remote Sens. 15, 105–122.
Coll, C., Caselles, V., Galve, J.M., Valor, E., Niclòs, R., Sánchez, J.M., 2006. Evaluation of split-window and dual-angle correction methods for land surface temperature retrieval from Envisat/Advanced along Track Scanning Radiometer (AATSR) data. J. Geophys. Res. 111, D12105.
Coll, C., Valor, E., Galve, J.M., Mira, M., Bisquert, M., García-Santos, V., Caselles, E., Caselles, V., 2012. Long-term accuracy assessment of land surface temperatures derived from the Advanced Along-Track Scanning Radiometer. Remote Sensing of Environment, Advanced Along Track Scanning Radiometer(AATSR) Special Issue. 116, 211–225.
Coppo, P., Ricciarelli, B., Brandani, F., Delderfield, J., Ferlet, M., Mutlow, C., Munro, G., Nightingale, T., Smith, D., Bianchi, S., Nicol, P., Kirschstein, S., Hennig, T., Engel, W., Frerick, J., Nieke, J., 2010. SLSTR: a high accuracy dual scan temperature radiometer for sea and land surface monitoring from space. J. Mod. Opt. 57, 1815–1830.
Duan, S.-B., Li, Z.-L., Wu, H., Leng, P., Gao, M., Wang, C., 2018. Radiance-based validation of land surface temperature products derived from Collection 6 MODIS thermal infrared data. Int. J. Appl. Earth Obs. Geoinf. 70, 84–92.
Ermida, S.L., Trigo, I.F., DaCamara, C.C., Göttsche, F.M., Olesen, F.S., Hulley, G., 2014. Validation of remotely sensed surface temperature over an oak woodland landscape-The problem of viewing and illumination geometries. Remote Sens. Environ. 148, 16–27.
François, C., Ottle, C., 1996. Atmospheric corrections in the thermal infrared: global and water vapor dependent split-window algorithms-applications to ATSR and AVHRR data. Ieee Trans. Geosci. Remote. Sens. 34, 457–470.
Freitas, S.C., Trigo, I.F., Bioucas-Dias, J.M., Gottsche, F.-M., 2010. Quantifying the uncertainty of land surface temperature retrievals from SEVIRI/Meteosat. IEEE Trans. Geosci. Remote Sens. 48, 523–534.
Galve, J.M., Coll, C., Caselles, V., Valor, E., 2008. An atmospheric radiosounding database for generating land surface temperature algorithms. Ieee Trans. Geosci. Remote. Sens. 46, 1547–1557.
Ghent, D.J., Corlett, G.K., Göttsche, F.-M., Remedios, J.J., 2017. Global land surface temperature from the Along-Track Scanning Radiometers. J. Geophys. Res. Atmos. 122 (12) 167-12,193.
Göttsche, F.-M., Hulley, G.C., 2012. Validation of six satellite-retrieved land surface emissivity products over two land cover types in a hyper-arid region. Remote Sens. Environ. 124, 149–158.
Göttsche, F.-M., Olesen, F.-S., Bork-Unkelbach, A., 2013. Validation of land surface temperature derived from MSG/SEVIRI with *in situ* measurements at Gobabeb, Namibia. Int. J. Remote Sens. 34, 3069–3083.
Göttsche, F.-M., Olesen, F.-S., Trigo, I., Bork-Unkelbach, A., Martin, M., 2016. Long Term Validation of Land Surface Temperature Retrieved from MSG/SEVIRI with Continuous*in-Situ* Measurements in Africa. Remote Sens. (Basel) 8, 410.
Guillevic, P.C., Biard, J.C., Hulley, G.C., Privette, J.L., Hook, S.J., Olioso, A., Göttsche, F.M., Radocinski, R., Román, M.O., Yu, Y., Csiszar, I., 2014. Validation of land surface temperature products derived from the Visible Infrared Imaging Radiometer Suite (VIIRS) using ground-based and heritage satellite measurements. Remote Sens. Environ. 154, 19–37.
Guillevic, P., Göttsche, F., Nickeson, J., Hulley, G., Ghent, D., Yu, Y., Trigo, I., Hook, S., Sobrino, J.A., Remedios, J., Román, M., Camacho, F., 2017. Land surface temperature product validation Best practice protocol. Version 1.0. In: Guillevic, P., Göttsche, F., Nickeson, J., Román, M. (Eds.), Best Practice for Satellite-Derived Land Product Validation (P. 60): Land Product Validation Subgroup (WGCV/CEOS), https://doi.org/10.5067/doc/ceoswgcv/lpv/lst.001.
Guo, G., Zhou, M., 2004. Using MODIS land surface temperature to evaluate forest fire risk of Northeast China. Ieee Geosci. Remote. Sens. Lett. 1, 98–100.

Hansen, M., DeFries, R., Townshend, J.R.G., Sohlberg, R., 1998. UMD Global Land Cover Classification, 1 Kilometer, 1.0 (1981-1994).
Huang, F., Zhou, J., Tao, J., Tan, X., Liang, S., Cheng, J., 2016. PMODTRAN: a parallel implementation based on MODTRAN for massive remote-sensing data processing. Int. J. Digit. Earth 9, 819–834.
Hulley, G.C., Hook, S.J., Baldridge, A.M., 2009a. Validation of the North American ASTER Land Surface Emissivity Database (NAALSED) version 2.0 using pseudo-invariant sand dune sites. Remote Sens. Environ. 113, 2224–2233.
Hulley, G.C., Hook, S.J., Manning, E., Lee, S.-Y., Fetzer, E., 2009b. Validation of the Atmospheric Infrared Sounder (AIRS) version 5 land surface emissivity product over the Namib and Kalahari deserts. J. Geophys. Res. 114, D19104. https://doi.org/10.1029/2009JD012351.
Hulley, G.C., Hook, S.J., Abbott, E., Malakar, N., Islam, T., Abrams, M., 2015. The ASTER Global Emissivity Dataset (ASTER GED): Mapping Earth's emissivity at 100 meter spatial scale. Geophys. Res. Lett. 42, 7966–7976. https://doi.org/10.1002/2015GL065564.
Jiang, G., Li, Z., 2008. Split-window algorithm for land surface temperature estimation from MSG1-SEVIRI data. Int. J. Remote Sens. 29, 6067–6074.
Jiang, G., Liu, R., 2014. Retrieval of sea and land surface temperature from SVISSR/FY-2C/D/E measurements. IEEE Trans. Geosci. Remote Sens. 52, 6132–6140.
Jiang, G., Zhou, W., Liu, R., 2013. Development of split-window algorithm for land surface temperature estimation from the VIRR/FY-3A measurements. IEEE Geosci. Remote Sensing Lett. 10, 952–956.
Jiménez-Muñoz, J.C., 2003. A generalized single-channel method for retrieving land surface temperature from remote sensing data. J. Geophys. Res. 108 (D22), 4688.
Kalma, J.D., McVicar, T.R., McCabe, M.F., 2008. Estimating land surface evaporation: a review of methods using remotely sensed surface temperature data. Surv. Geophys. 29, 421–469.
Li, Z., Jia, L., Su, Z., Wan, Z., Zhang, R., 2003. A new approach for retrieving precipitable water from ATSR2 split-window channel data over land area. Int. J. Remote Sens. 24, 5095–5117.
Li, Z., Tang, B., Wu, H., Ren, H., Yan, G., Wan, Z., Trigo, I.F., Sobrino, J.A., 2013a. Satellite-derived land surface temperature: current status and perspectives. Remote Sens. Environ. 131, 14–37.
Li, Z., Wu, H., Wang, N., Qiu, S., Sobrino, J.A., Wan, Z., Tang, B.-H., Yan, G., 2013b. Land surface emissivity retrieval from satellite data. Int. J. Remote Sens. 34, 3084–3127.
Li, X., Cheng, G., Liu, S., Xiao, Q., Ma, M., Jin, R., Che, T., Liu, Q., Wang, W., Qi, Y., Wen, J., Li, H., Zhu, G., Guo, J., Ran, Y., Wang, S., Zhu, Z., Zhou, J., Hu, X., Xu, Z., 2013c. Heihe water allied telemetry experimental research (HiWATER): scientific objectives and experimental design. Bull. Am. Meteorol. Soc. 94, 1145–1160.
Li, M., Zhou, J., Peng, Z., Liu, S., Göttsche, F.-M., Zhang, X., Song, L., 2019. Component radiative temperatures over sparsely vegetated surfaces and their potential for upscaling land surface temperature. Agric. For. Meteorol. 276–277, 107600.
Liang, S., 2005. Quantitative Remote Sensing of Land Surfaces. John Wiley & Sons.
Liu, S., Xu, Z., Wang, W., Jia, Z., Zhu, M., Bai, J., Wang, J., 2011. A comparison of eddy-covariance and large aperture scintillometer measurements with respect to the energy balance closure problem. Hydrol. Earth Syst. Sci. 15 (4), 1291–1306.
Liu, Y., Yu, Y., Yu, P., Göttsche, F., Trigo, I., 2015. Quality assessment of S-NPP VIIRS land surface temperature product. Remote Sens. (Basel) 7, 12215–12241.
Liu, S., Li, X., Xu, Z., Che, T., Xiao, Q., Ma, M., Liu, Q., Jin, R., Guo, J., Wang, L., Wang, W., Qi, Y., Li, H., Xu, T., Ran, Y., Hu, X., Shi, S., Zhu, Z., Tan, J., Zhang, Y., Ren, Z., 2018. The heihe integrated observatory network: a basin-scale land surface processes observatory in China. Vadose Zone J. 17, 180072.
Ma, Y., Tsukamoto, O., 2002. Combining Satellite Remote Sensing With Field Observations for Land Surface Heat Fluxes Over Inhomogeneous Landscape. China Meteorological Press, Beijing.
Masuda, K., Takashima, T., Takayama, Y., 1988. Emissivity of pure and sea waters for the model sea surface in the infrared window regions. Remote Sens. Environ. 24, 313–329.
Olsen, E.T., Fishbein, E., Granger, S., Lee, S.Y., Manning, E., et al., 2007. AIRS/AMSU/HSB Version 5 Data Release User Guide. Jet Propulsion Laboratory, California Institute of Technology, Pasadena, CA.
Ottlé, C., Vidal-Madjar, D., 1992. Estimation of land surface temperature with NOAA9 data. Remote Sens. Environ. 40, 27–41.
Pearson, R.K., 2002. Outliers in process modeling and identification. Ieee Trans. Control. Syst. Technol. 10, 55–63.
Peres, L.F., DaCamara, C.C., 2005. Emissivity maps to retrieve land-surface temperature from MSG/SEVIRI. Ieee Trans. Geosci. Remote. Sens. 43, 1834–1844.
Prata, F., 2002. Land Surface Temperature Measurement From Space: AATSR Algorithm Theoretical Basis (Contract Report to ESA). CSIRO Atmospheric Research, Aspendale, Victoria, Australia.
Prata, A.J., Platt, C.M.R., 1991. Land surface temperature measurements from the AVHRR. In: Presented at the 5th AVHRR Data Users Conference. Tromso, Norway. pp. 433–438.
Price, J.C., 1984. Land surface temperature measurements from the split window channels of the NOAA 7 Advanced very High Resolution Radiometer. J. Geophys. Res. Atmos. 89, 7231–7237.
Qin, Z., Karnieli, A., Berliner, P., 2001. A mono-window algorithm for retrieving land surface temperature from Landsat TM data and its application to the Israel-Egypt border region. Int. J. Remote Sens. 22, 3719–3746.
Remedios, J., et al., 2012. Sentinel-3 Optical Products and Algorithm Definition Land Surface Temperature. pp. 24.
Ren, H., Ye, X., Liu, R., Dong, J., Qin, Q., 2018. Improving land surface temperature and emissivity retrieval from the chinese Gaofen-5 satellite using a hybrid algorithm. IEEE Trans. Geosci. Remote Sens. 56, 1080–1090.
Sentinel-3 team, 2013. Sentinel-3 User Handbook. pp. 117.
Sobrino, J., 2001. A comparative study of land surface emissivity retrieval from NOAA data. Remote Sens. Environ. 75, 256–266.
Sobrino, J.A., Raissouni, N., 2000. Toward remote sensing methods for land cover dynamic monitoring: application to Morocco. Int. J. Remote Sens. 21, 353–366.
Sobrino, J., Coll, C., Caselles, V., 1991. Atmospheric correction for land surface temperature using NOAA-11 AVHRR channels 4 and 5. Remote Sens. Environ. 38, 19–34.
Sobrino, J., Jimenezmunoz, J., Verhoef, W., 2005. Canopy directional emissivity: comparison between models. Remote Sens. Environ. 99, 304–314.
Sobrino, J.A., Jiménez-Muñoz, J.C., Sòria, G., Ruescas, A.B., Danne, O., Brockmann, C., Ghent, D., Remedios, J., North, P., Merchant, C., Berger, M., Mathieu, P.P., Göttsche, F.-M., 2016. Synergistic use of MERIS and AATSR as a proxy for estimating Land Surface Temperature from Sentinel-3 data. Remote Sens. Environ.
Tang, B., Bi, Y., Li, Z.-L., Xia, J., 2008. Generalized split-window algorithm for estimate of land surface temperature from chinese geostationary FengYun meteorological satellite (FY-2C) data. Sensors. 8, 933–951.
Tang, B., Shao, K., Li, Z.-L., Wu, H., Nerry, F., Zhou, G., 2015. Estimation and validation of land surface temperatures from chinese second-generation polar-orbit FY-3A VIRR data. Remote Sens. (Basel) 7, 3250–3273.
Theocharous, E., Fox, N.P., Barker-Snook, I., Nicl, R., Santos, V.G., Minnett, P.J., 2019. The 2016 CEOS Infrared Radiometer Comparison: Part II: Laboratory Comparison of Radiation Thermometers. J. Atmos. Oceanic Technol. 36, 1079–1092.
Tomlinson, C.J., Chapman, L., Thornes, J.E., Baker, C., 2011. Remote sensing land surface temperature for meteorology and climatology: a review: remote sensing land surface temperature. Meteorol. Appl. 18, 296–306.
Ulivieri, C., Cannizzaro, G., 1985. Land surface temperature retrievals from satellite measurements. Acta Astronaut. 12, 977–985.
Ulivieri, C., Castronuovo, M.M., Francioni, R., Cardillo, A., 1994. A split window algorithm for estimating land surface temperature from satellites. Adv. Space Res. 14, 59–65.
Vidal, A., 1991. Atmospheric and emissivity correction of land surface temperature measured from satellite using ground measurements or satellite data. Int. J. Remote Sens. 12, 2449–2460.
Wan, Z., 2014. New refinements and validation of the collection-6 MODIS land-surface temperature/emissivity product. Remote Sens. Environ. 140, 36–45.
Wan, Z., Dozier, J., 1996. A generalized split-window algorithm for retrieving land-surface temperature from space. Ieee Trans. Geosci. Remote. Sens. 34, 892–905.
Wan, Z., Li, Z.-L., 1997. A physics-based algorithm for retrieving land-surface emissivity and temperature from EOS/MODIS data. IEEE Trans. Geosci. Remote Sens. 35, 980–996.
Wan, Z., Wang, P., Li, X., 2004. Using MODIS Land Surface Temperature and Normalized Difference Vegetation Index products for monitoring drought in the southern Great Plains, USA. Int. J. Remote Sens. 25, 61–72.
Wang, M., He, G., Zhang, Z., Wang, G., Wang, Z., Yin, R., Cui, S., Wu, Z., Cao, X., 2019. A radiance-based split-window algorithm for land surface temperature retrieval: Theory and application to MODIS data. Int. J. Appl. Earth Obs. Geoinf. 76, 204–217.
Weng, Q., 2009. Thermal infrared remote sensing for urban climate and environmental studies: methods, applications, and trends. Isprs J. Photogramm. Remote. Sens. 64, 335–344.
Xu, Z., Liu, S., Li, X., Shi, S., Wang, J., Zhu, Z., Xu, T., Wang, W., Ma, M., 2013. Intercomparison of surface energy flux measurement systems used during the HiWATER-MUSOEXE. J. Geophys. Res. Atmos. 118 (13) 140–13,157.
Ye, X., Ren, H., Liu, R., Qin, Q., Liu, Y., Dong, J., 2017. Land surface temperature estimate from chinese Gaofen-5 satellite data using split-window algorithm. IEEE Trans. Geosci. Remote Sens. 55, 5877–5888.
Yu, Y., Privette, J.L., Pinheiro, A.C., 2005. Analysis of the NPOESS VIIRS land surface temperature algorithm using MODIS data. Ieee Trans. Geosci. Remote. Sens. 43, 2340–2350.
Yu, Y., Privette, J.L., Pinheiro, A.C., 2008. Evaluation of split-window land surface temperature algorithms for generating climate data records. Ieee Trans. Geosci. Remote. Sens. 46, 179–192.
Yu, Y., Tarpley, D., Privette, J.L., Flynn, L.E., Xu, H., Chen, M., Vinnikov, K.Y., Sun, D., Tian, Y., 2012. Validation of GOES-R satellite land surface temperature algorithm using SURFRAD ground measurements and statistical estimates of error properties. IEEE Trans. Geosci. Remote Sens. 50, 704–713.
Yu, Y., Liu, Y., Yu, P., Liu, Y., Yu, P., 2018. Land surface temperature product development for JPSS and GOES-R missions. Comprehensive Remote Sensing. Elsevier, pp. 284–303.
Zhang, S., Duan, S.-B., Li, Z.-L., Huang, C., Wu, H., Han, X.-J., Leng, P., Gao, M., 2019. Improvement of split-window algorithm for land surface temperature retrieval from Sentinel-3A SLSTR data over barren surfaces using ASTER GED product. Remote Sens. (Basel) 11, 3025.
Zheng, Y., Ren, H., Guo, J., Ghent, D., Tansey, K., Hu, X., Nie, J., Chen, S., 2019. Land surface temperature retrieval from Sentinel-3A sea and land surface temperature radiometer, using a split-window algorithm. Remote Sens. (Basel) 11, 650.
Zhou, J., Li, J., Zhang, L., Hu, D., Zhan, W., 2012. Intercomparison of methods for estimating land surface temperature from a Landsat-5 TM image in an arid region with low water vapour in the atmosphere. Int. J. Remote Sens. 33, 2582–2602.
Zhou, J., Li, M., Liu, S., Jia, Z., Ma, Y., 2015. Validation and performance evaluations of methods for estimating land surface temperatures from ASTER data in the middle reach of the Heihe River Basin, Northwest China. Remote Sens. (Basel) 7, 7126–7156.
Zhou, J., Liang, S., Cheng, J., Wang, Y., Ma, J., 2019. The GLASS land surface temperature product. Ieee J. Sel. Top. Appl. Earth Obs. Remote. Sens. 12, 493–507.